TAMPEREEN TEKNILLINEN YLIOPISTO
TAMPERE UNIVERSITY OF TECHNOLOGY

DEFNE US

METAL ARTIFACT REDUCTION IN SINOGRAMS OF DENTAL COMPUTED TOMOGRAPHY

Master of Science Thesis

Examiners: Prof. Ulla Ruotsalainen
Prof. Jari Viik
M.Sc. Uygar Tuna
Examiners and topic approved by the Faculty Council of Natural Sciences on 3rd of April 2013.

ABSTRACT

TAMPERE UNIVERSITY OF TECHNOLOGY
International Master's Degree Programme in Biomedical Engineering
US, DEFNE: Metal Artifact Reduction in Sinograms of Dental Computed Tomography
Master of Science Thesis, 70 pages, 4 Appendix pages
May 2013
Major subject: Biomedical Engineering
Examiners: Prof. Ulla Ruotsalainen
Prof. Jari Viik
M.Sc. Uygar Tuna
Keywords: Cone-beam computed tomography (CBCT), Discrete Cosine Transform (DCT), gap filling methods, jaw tilting, metal artifacts, segmentation

Use of metal objects such as dental implants, fillings, crowns, screws, nails, prosthesis and plates have increased in dentistry over the past 20 years, which raised a need for new methods for reducing the metal artifacts in medical images. Although there are several algorithms for metal artifact reduction, none of these algorithms are efficient enough to recover the original image free of all artifacts.

This thesis presents two approaches for reducing metal artifacts through accurate segmentation of metal objects on dental computed tomography images. First approach was based on construction and tilting of a 3D jaw phantom, aiming to obtain fewer metals on each slice. 3D jaw phantom included the main anatomical structures of a jaw, and multiple metal fillings inserted on the teeth. Each jaw slice on the 3D phantom was tilted in order to mimic the (1) nodding movement, and (2) mouth opening/closing. Second approach was to segment the metals on an experimental dataset, consisting of a Cone-Beam Computed Tomography image, by using different segmentation algorithms. K-means clustering, Otsu's thresholding method and logarithmic enhancement were used for extracting the metals from a real dental CT slice. Once the metal fillings on the jaw phantom were segmented out from the image, they were compensated by gap filling methods; Discrete Cosine Domain Gap Filling and inpainting.

Qualitative and quantitative analyses were carried out for evaluating the performance of implemented segmentation methods. Efficiency of tilting alternatives on the segmentation of metal fillings was compared. In conclusion, jaw opening/closing movement between 24º-30º suggested a significant enhancement in segmentation, thus, metal artifact reduction on the jaw phantom. Inpainting method showed a better performance for both simulated and experimental dataset over the DCT domain gap filling method. Moreover, merging the logarithmic enhancement and inpainting showed superior results over other metal artifact reduction alternatives.

PREFACE

This work has been conducted in the Methods and Models for Biological Signals and Images (M^2oBSI) research group, at the Department of Signal Processing, Tampere University of Technology, Finland.

Firstly, I would like to express my gratitude to my supervisors Prof. Ulla Ruotsalainen and MSc. Uygar Tuna for providing me the chance to work on such an interesting and instructive project, and for their extensive supervision and support throughout the thesis work. I would also like to thank Prof. Jari Viik for his supervision in leading me towards the project and his guidance during my studies.

I would owe my gratitude to my family, my mother Deniz Us, my father Hakan Us, my grandfather Necdet Tuna, and my grandmother Şahızenan Tuna for being by my side at all times, encouraging me to go further in life with their valuable experiences and advices.

I also give my special thanks to Javier Lopez, for his moral support, patience and understanding over the course of this thesis. Also I am grateful to Artur Sossin for his valuable feedback and ideas that inspired me during the project.

Tampere, May 2013.

Defne Us

Insinöörinkatu 60 B 109 C

33720 Tampere, FINLAND

+358 443493991

defne.us@tut.fi

LIST OF SYMBOLS

$A(\tau,\varphi)$	Ray integral
$B\{\cdot\}$	Backprojection operator
δ	Dirac delta function
f	Frequency
f_m	Maximum frequency
f(x,y)	Scanned object in spatial domain with coordinates (x,y)
$\hat{f}(x, y)$	Reconstructed value of f(x,y) in spatial domain
F(u,v)	2D Fourier transform of f(x,y)
$F_0(w,\phi)$	Polar form of F(u,v), w being the distance from origin and ϕ is the angle
$\hat{g}$ (x,y)	Reconstructed image
g (x,y)	Original image
σ_i	Variance of class i
σ_w	Weighted sum of variances
H	Calculated Hounsfield unit value
HU	Hounsfield Unit
H(f)	Hann window
$I_m(\tau)$	Measured intensity by detectors
I_0	Initial ray intensity
μ	Linear attenuation coefficient (m^{-1})
$\mu_i(t)$	Mean value of class i
$\mu_B(T)$	Average of four corner pixels
$\mu_0(T)$	Average of all pixels except corners
N	Number of detectors
$P_\varphi(s)$	Projection vector at angle φ
$p(\varphi,s)$	Radon transform of f(x,y)
$P_\varphi(v)$	1D Fourier transform of $P_\varphi(s)$

$R\{\cdot\}$	Radon Transform operator
s	Distance from origin
t	Threshold
φ	Projection angle
w_i	Probability of the two classes separated by a threshold t
x	Thickness of an object
(x_0,y_0)	Known pixel values at coordinates (x_0,y_0)
(x_1,y_1)	Known pixel values at coordinates (x_1,y_1)

LIST OF ABBREVIATIONS

1D	1 Dimensional
2D	2 Dimensional
3D	3 Dimensional
ART	Algebraic reconstruction algorithm
BP	Backprojection
CBCT	Cone-beam computed tomography
CT	Computed tomography
COR	Center of rotation
DICOM	Digital imaging and communications in medicine
DCT	Discrete cosine transform
DMF	Dento-maxillofacial
FBP	Filtered backprojection
FDK	Feldkamp-David-Kress
FOV	Field of view
FT	Fourier Transform
HU	Hounsfield Units
HVS	Human visual system
IDCT	Inverse discrete cosine transform
kVp	Peak voltage in kilovolts
MAR	Metal artifact reduction
MDCT	Medical CT
MLEM	Maximum likelihood estimation maximization
MPR	Metal projection region
MSE	Mean squared error
µSV	Micro Sievert
NMSE	Normalized mean squared error

SNR	Signal-to noise ratio
SSIM	Structural similarity
ROI	Region of interest
RT	Radon transform
PET	Positron emission tomography
PSF	Point spread function
PSNR	Peak signal-to-noise ratio

TABLE OF CONTENTS

1. INTRODUCTION

Metal implants inside the body cause artifacts in medical images, preventing the accurate observations on the subject. In this context, the term artifact describes a mismatch between the intensity values of the reconstructed image and the true attenuation coefficients of the object, which is especially large for high density objects such as metals [1]. Several algorithms and techniques have been developed to reduce metal artifacts, and they are collectively called as Metal Artifact Reduction (MAR) techniques. Unfortunately, these techniques are mostly target specific artifact sources arising from the existence of the metals, thus there is not a standard method in clinical use.

Within the United States alone, it is estimated that each year 300,000 metal implants are placed with the contribution of more than 50 companies involved in the manufacturing, marketing and distribution processes [2]. Large number of metal implants used in contemporary dentistry creates an important field for research, aiming to reduce the artifacts arising from these metals. Also estimated market value of implant dentistry for 2020 is around 4.8-6.5 billion euros with an approximate growth rate of 6-10% since 2011 [3]. This growth can be explained by the expected increase in affordability, accessibility and acceptance of dental implants in the society.

All imaging modalities are affected from the existence of metals inside the body; including planar imaging, X-ray Computed Tomography (CT), Positron Emission Tomography (PET) and magnetic resonance imaging (MRI). Among these, X-ray CT is the most commonly used modality in dental imaging because of its superior image resolution for visualization of hard and soft tissues, low noise and relatively fast scanning time. Due to the common use of high density objects in dental CTs, MAR for dental images become a major research interest. This is the case especially for dental restorations and orthodontic applications, in which various kinds of metals are involved in the procedures, including stainless steel, gold alloys, silver amalgam, platinum, lead, tin and aluminum [4]. While the ideal approach for MAR would simply be physically removing all metal substances in oral cavity, in case of crowns, bridges and dental implants, it is not always possible [5]. Therefore, dental CT images have to be post-processed by MAR techniques. MAR can be especially difficult in the case of dental images obtained by CBCT because (1) area surrounding the metal implants (crowns, fillings or braces) is small in dental cases, making it difficult to estimate the bin values and (2) CBCT uses less radiation dose than conventional X-ray CTs, causing the images to be more prone to artifacts caused by high density objects like metals.

This thesis aims at obtaining the best MAR by segmentation of metals and replacement of the segmented metallic regions by using gap filling algorithms. While segmentation methods try to extract the metallic regions from the image, gap filling methods are based on the principle of estimating the segmented regions as accurately as possible via interpolation of neighboring pixels. In order to obtain good results from the gap filling methods, accurate segmentation of metals is crucial. However, segmentation methods often result in inaccurate reconstruction if there are great amount of metals or amount of data around the metallic regions are too little. Therefore, this thesis evaluates

the performance of different segmentation algorithms and gap filling methods on a simulated 3D jaw phantom and an experimental dataset obtained from CBCT. In addition to the comparisons of segmentation and gap-filling methods, this thesis also investigates the effect of jaw tilting on reconstruction qualities of CBCT images as an attempt to improve image quality. The purpose of this tilting is to avoid the coplanarity of teeth and metals by having the metals and teeth on different planes, as well as avoiding the overlap of the metals in the projections [6].

2. PRINCIPLES OF X-RAY COMPUTED TOMOGRAPHY

X-ray Computed Tomography (X-ray CT) was the first imaging modality that was based on solely digital reconstruction; therefore, it has an historical importance in medical imaging. Since its first development, X-ray CT has been constantly improved with new additions and modifications, trying to achieve faster imaging time, lower radiation dose and better image quality. As it is also mentioned in [7], among all contemporary CTs, X-ray CT is the most common CT modality that provides images with excellent spatial resolution, along with an acquisition time close to real-time imaging. Increasing power of the computers and high technology detectors enables us to obtain low dose images in a short sequence from X-ray CTs; information needed for a full 3D volume can be gathered within 30 seconds to a few minutes acquisition [8].

One of the most frequent use of X-ray CTs are in orthodontic assessments because it can provide immediate and accurate two-dimensional (2D) and three dimensional (3D) radiographic structures, only limited with the selected field of view (FOV) [8]. Similar to other digital radiographic imaging modalities, CT electronically records X-rays that are not attenuated during the transmission through tissues of the patient. An example of a commercial CT and its schematic representation are depicted in Figure 2.1.

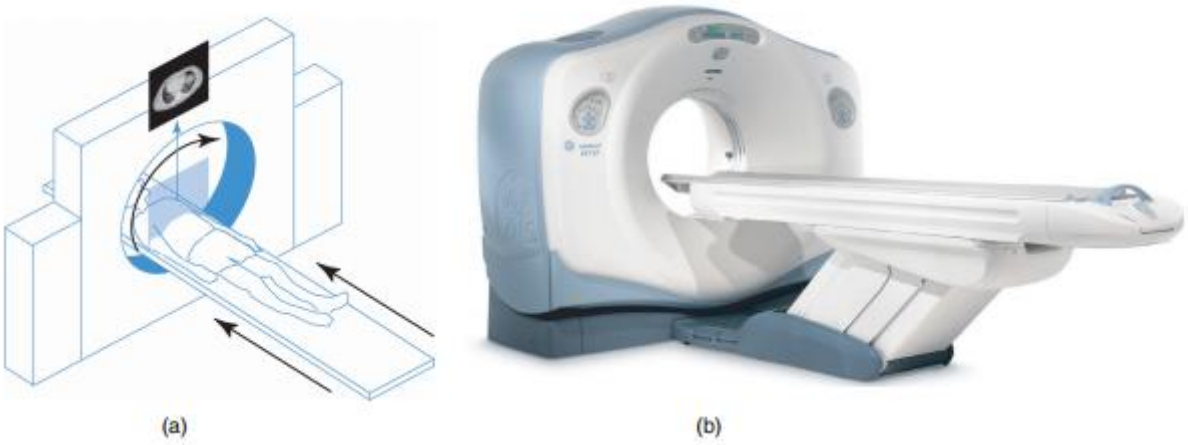

Figure 2.1: (a) Schematic representation and (b) photograph of a CT scanner (Courtesy of GE Healthcare).

In CT measurements, CT intensity values are measured with Hounsfield Units (HU). HU represents the amount of X-ray attenuation of the beam caused by the scanned object, providing a basis for quantitative assessment of bone density. Depending on the HU values, tissue properties such as bone mineral density, lung nodule calcification and tissue blood flow can be quantified [9]. Calculation of HU is shown in (1), where μ is the linear attenuation coefficient and H is the corresponding HU.

$$H = \frac{\mu - \mu_{water}}{\mu_{water}} \times 1000 \quad (1)$$

Density of the material has a linear effect on μ, leading to higher attenuation for high density objects. Usual range of HU obtained from CT scanners is between -1000 and 3000, where -1000 corresponds to the attenuation coefficient of air (μ=0) and 3000 for dense bone. [10]

2.1. Image Acquisition in Computed Tomography

CT is based on the same physical principles as radiography. It uses an external thin X-ray source, where a set of lines is scanned through the FOV. This process is repeated for various angles, gathering line attenuation values from all possible angles and all possible distances from the center. Similar to other 2D images, CT images are also composed of "pixels," which are elements arranged in a 2D rectangular matrix [8]. Each pixel has an intensity value, denoting the amount of attenuation in the X-ray beam, as well as its location in the matrix. Based on these attenuation values, actual attenuation values at all points are reconstructed [11]. Non-linear attenuation of X-rays (I_m) is calculated as follows:

$$I_m = I_0 e^{-\mu x}, \quad (2)$$

where I_0 is the original photon count formed by the beam, μ is the linear attenuation coefficient (m^{-1}) and x is the thickness of the object [7]. Integral of attenuation for each ray position τ, defined as ray integral, is given as

$$A(\tau) = \int_{r=0}^{r_p} \mu(\tau, r)\, dr = \log \frac{I_m(\tau)}{I_0}, \quad (3)$$

Where $I_m(\tau)$ represents the measured intensity by the detectors, whereas I_0 is the initial ray intensity [7]. X-rays can be parallel or fan-shaped depending on the CT model, and the ray integral profile for the conventional parallel beam geometry is depicted in Figure 2.2.

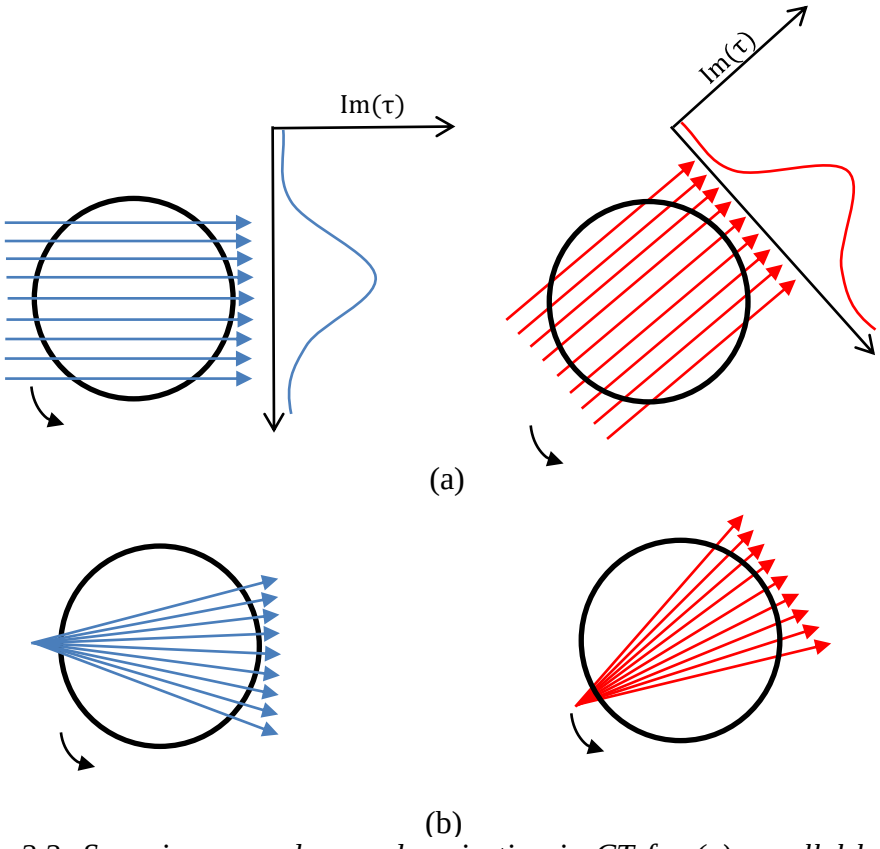

Figure 2.2: Scanning procedure and projection in CT for (a) parallel beam geometry and (b) fan beam geometry. Although the measured intensities are only shown for parallel beam geometry, they follow a similar pattern for fan beams in (b).

When these ray integrals $A(\tau)$ are computed over several angles, equation (3), which was one dimensional (1D), becomes a 2D case [7]. This 2D form represents the line attenuation integrals over all possible angles and distances from the center, also called Radon Transform (RT), whose properties is explained further in the following section.

2.2.1. 2D Radon Transform

Radon Transform (RT), also called forward projection, is one of the major concepts in image reconstruction, especially in medical imaging, where the RT is essential for images acquisition [12]. RT is based on interpreting an object by integration of 2D line integrals, which represents the integral of certain parameter along a line, at a specific angle of rotation. In the case of CT, these line integrals represent the attenuation of X-rays travelling through the object as a line. An X-ray CT scanner system is depicted in Figure 2.3, where beams travelling from the source to the detector are drawn as arrows, which are later processed by computer and visualized as a slice view.

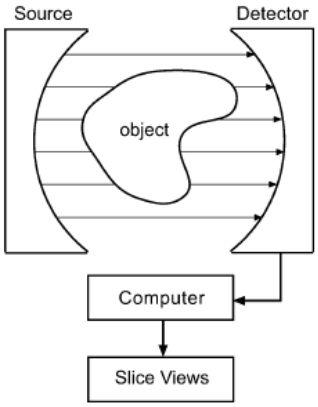

Figure 2.3: X-ray CT scanning system. Rays passing through the object from the source to detector are acquired and processed by the computer, translated into slice views [12].

Each ray passing through the object from source to detector in Figure 2.3, creates 1D line integrals at each angle of rotation as demonstrated in Figure 2.4. When these line integrals are stacked together, they form a projection vector $p_\varphi(s)$ at a specific angle.

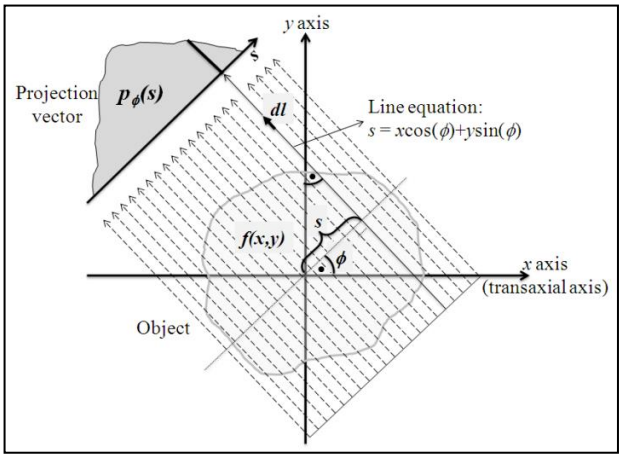

Figure 2.4: Generation of a projection vector. Line integrals through an object at a specific angle collectively form the projection vector, which is defined by the angle between the transaxial axis and the line, as well as the distance from the origin [13].

Projection vector $p_\varphi(v)$ can be measured by moving an X-ray source and detector on opposite sides along parallel lines of an object and $p_\varphi(s)$ can be formulated as follows:

$$p_\varphi(s) = \int_{(s,\varphi)\,\mathrm{line}} f(x,y)\,dl\,, \quad (4)$$

where s is the distance between the line and the origin of the coordinate system , φ is the angle between the y-axis and $f(x,y)$ is the scanned object in Cartesian coordinate system.

In the case of 2D reconstruction, the problem is to recover $p(\varphi,s)$ from $f(x,y)$. In order to do so, these projection vectors are stacked through a range of angles (limited by the maximum angle of the scanner), for all the radial samples. This transform is called Radon Transform and denoted by

$$R(f(x,y)) = p(\varphi, s) = \int_{-\infty}^{\infty}\int_{-\infty}^{\infty} f(x,y)\,\delta(x\cos\varphi + y\sin\varphi - \tau)\,dx\,dy \quad (5)$$

Where *p(φ,s)* is the RT of *f(x,y)*. Three projection vectors at angles 0 (view 1), π/4 (view 2) and π/2 (view 3) are depicted in Figure 2.5, where each view represents a single row/column in a sinogram. When these projection vectors are stacked together in the order of their acquisition angles, they create the sinogram slice for that object.

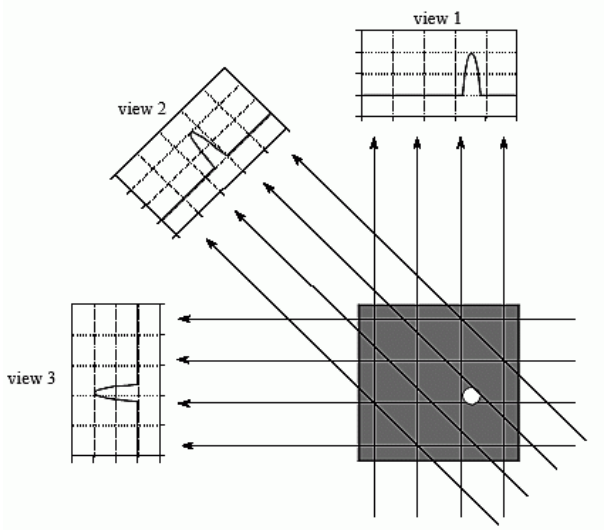

Figure 2.5: CT views at 0 (view 1), π/4 (view 2) and π/2 (view 3) generated by the line integrals through an object [14].

2.2.2. Sinogram

If we use *s* and *φ* as vertical and horizontal axes respectively, then when a Dirac impulse is displayed as projections $P_\varphi(s)$, resulting image is a sinusoid corresponding to the function

$$s = x_0\cos\varphi + y_0\sin\varphi \quad (6)$$

Each point (x,y) has the value of $\sqrt{x^2 + y^2}$, *s* being the distance from the origin, and the phase of the sinusoid depending on *φ*. A sinogram consists of weighted average of these sinusoids by the value of *f(x,y)* [15]. The sinusoidal trajectory in the sinograms and line integrals taken from two angles (π/2, π/4) are shown in Figure 2.6.

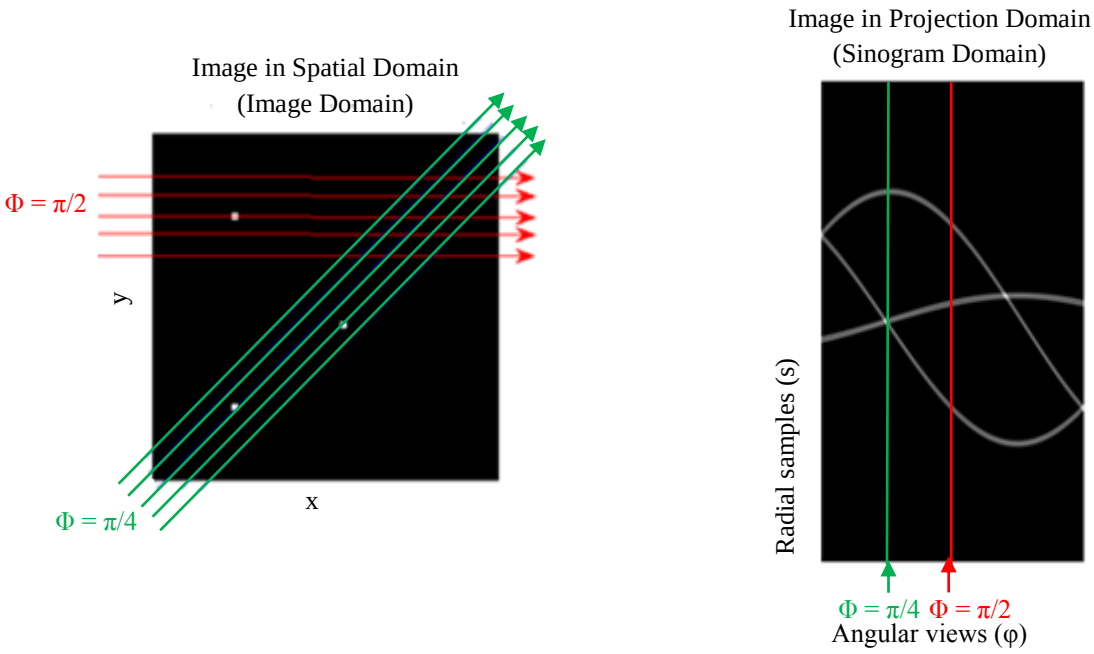

Figure 2.6: Sinogram generation from (a) spatial domain to (b) projection domain. Example line integrals are shown for Φ=π/2 and Φ=π/4 in the figure [10].

2.2.3. Fourier-slice Theorem

Fourier-slice theorem, also known as *central slice theorem* or *projection-slice theorem*, plays an important role in understanding the image reconstruction in CT, and it relates the 2D Fourier Transform (FT) of an image to the 1D FT of its projection. Let *f(x,y)* be a two-dimensional function, and $P_\varphi(s)$ is the Radon Transform of *f(x,y)* that was previously defined in (5), and 1D FT of $P_\varphi(s)$ is denoted with $P_\varphi(v)$, then $P_\varphi(v)$ can be formulated as

$$p_\varphi(v) = \int_{-\infty}^{\infty} p_\varphi(s) e^{-i2\pi vs} ds. \quad (7)$$

Correlation between $P_\varphi(s)$ and $P_\varphi(v)$ expressed in (7) shows that 1D projection of an image at an angle φ corresponds to the profile through the 2D FT of the object at the same angle, $P_\varphi(v)$. If *F(u,v)* is used to represent the 2D FT of *f(x,y)* with u = w cosφ and v=w sinφ, then *F(u,v)* can be written as follows:

$$F(u,v) = \int_{-\infty}^{\infty}\int_{-\infty}^{\infty} f(x,y) e^{-i2\pi(ux+vy)} dxdy. \quad (8)$$

(8) denotes the transformation of all projections into 2D Fourier plane. After obtaining the full FT of the object, recovery of the object can be accomplished by using the inverse FT. By combining (7) and (8), now Fourier-slice theorem can be defined as

$$P_{\varphi}(w) = F(w\cos\varphi, w\sin\varphi) = F_0(w,\varphi), \forall w \in R, \forall \varphi \in R, \quad (9)$$

Where $F_0(w,\varphi)$ stands for the polar form of $F(u,v)$ [15]. From (9), it can be deduced that any object $f(x,y)$ with an existent FT can be recovered by an inverse 2D FT because there is a one-to-one correspondence between the RT and 2D FT $F(u,v)$ and any object $f(x,y)$ can be described by its RT [16].

2.2. CT Reconstruction from Sinograms

Since Radon Transform does not have an exact inversion in practical applications, an approximate method has to be used for reconstruction of relative linear attenuation values in X-ray CT. Image reconstruction methods, used in MAR, are explained further in Chapter 7.

The simplest and the most commonly used analytical reconstruction method is referred as backprojection (BP), which tries to recover the object $f(x,y)$ from $P_{\varphi}(s)$ by smearing each sinogram back into spatial domain along a corresponding ray, *i.e.* acquiring CT images from its projections.

$$B\{R\{f(x,y)\}\} = \hat{f}(x,y) = \int_0^{\pi} p(x\cos\varphi + y\sin\varphi)\,d\varphi \quad (10)$$

where $\hat{f}(x,y)$ is the estimated values in spatial domain [17]. Depending on the number of projection vectors (angles), BP performance varies significantly. Effect of the number of angles used in BP is shown in Figure 2.7, where reconstruction quality of the Shepp-Logan phantom increases significantly as the number of projections increase.

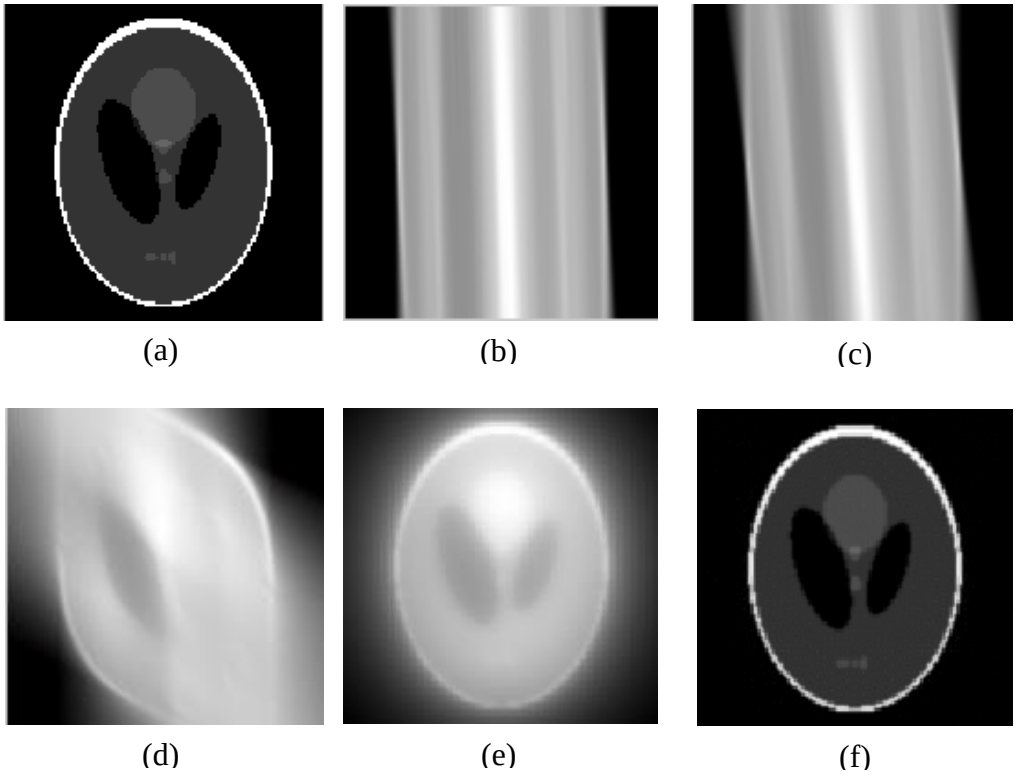

Figure 2.7: (a) Original Shepp-Logan phantom, (b-c-d-e) unfiltered backprojected images with 4, 8, 64, and 128 projections, (f) reconstructed image with filtered backprojection with 128 projections. Blurred edges of unfiltered images in (e) seem much sharper after filtering in (f).

As it is explained in [17], BP results do not correspond to the exact attenuation values due to non-dimensionality of values in the projection domain. Although BP is an efficient and fast algorithm, it results in blurred images. Blurring effect in the image can be formulated as follows:

$$\hat{f}(x, y) = f(x, y) * \frac{1}{\sqrt{(x^2 + y^2)}} \quad (11)$$

where *f(x,y)* is function representing the real attenuation values and $\frac{1}{\sqrt{(x^2+y^2)}}$ is the point spread function (PSF). These two functions are convolved with the convolution operation shown with "*" in (11) [18]. Effect of PSF on a simple Shepp-Logan image can be seen in Figure 2.7.e. In order to decrease the blurring effect, filtered back projection (FBP) is used, which is a modified BP algorithm followed by an additional filtering step, where projections are passed through a high-pass filter. Via filtering, the edges of the image become sharper, compensating the effect of blurring. Deblurring effect of filtering can be clearly seen in Figure 2.7.f, in which the filter provides sharper edges for the object than Figure 2.7.e. Different filters in a pre-determined window can be used depending on the purpose of reconstruction. It is shown in Figure 2.7 that sharp filters such as RamLak filter result in sharp edges by amplifying the high frequency components while suppressing the low frequencies. However, this high frequency amplification also causes the amplification of the noise. Filters such as Hamming filter have lower slopes than RamLak, which results in smoother images, with less noise

amplification, but at the cost of edge sharpness. One should note that filters used in FBP are applied inside a certain bandwidth in order to satisfy the Nyquist rate [7].

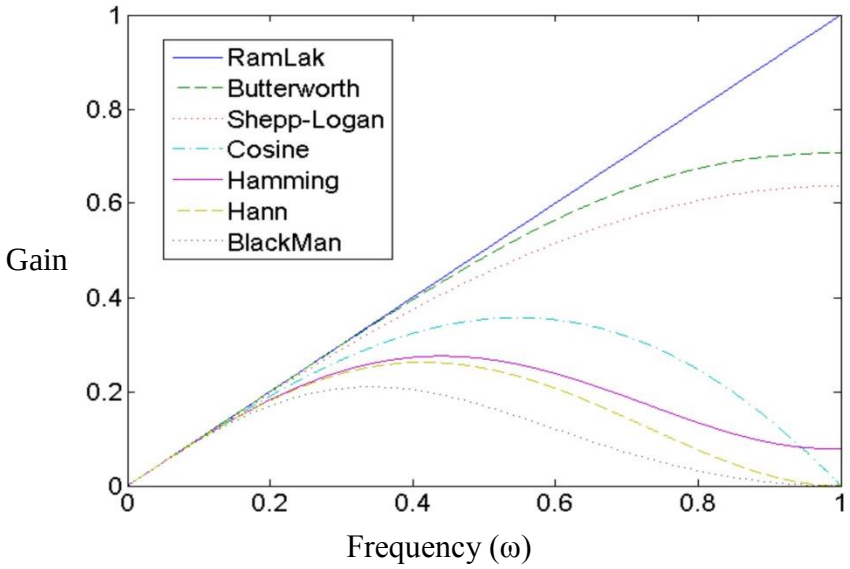

Figure 2.8: Different filters used in FBP. RamLak filter has the highest slope, providing provides the sharpest filtering, but also with the highest amplification of high frequency noise. BlackMan filter has the lowest slope in the figure, therefore, it amplifies the noise the least, but it does not provide an effective filtering effect [19].

In the context of this thesis, bicubic interpolation was utilized in FBP due to the use of large amount of neighbors (16 neighbors in the closest 4x4 neighborhood) in the calculation of a pixel value, which makes the interpolated images smoother, as well as decreasing the visible artifacts caused by BP.

In this thesis, Hann (Hanning) filter was selected as the window function for FBP. A Hann window is defined with the following formula

$$H(f) = \begin{cases} 0.5 + 0.5\cos\left(\frac{\pi f}{f_m}\right), 0 \le |f| \le f_m \\ 0, \text{otherwise} \end{cases} \quad (12)$$

Due to its smooth shape and fast convergence to zero, Hann filter is very useful to reduce noise and obtain a smooth image in backprojection, which is also the reason why it is used in the context of this thesis.

2.3. Evolution of Computed Tomography

First Generation: First modern CT was installed and used for clinical purposes by an engineer in British EMI Corp, called Godfrey Hounsfield in 1971 [20]. First CT, designed by Hounsfield, was able to measure 160 X-ray beams per each set of translation, and according to Goldman *et al.*, this number has been increased to an average of 750 beams with the improvements in the CT technology over the years. After the completion of each translation set, the scanner rotated around the subject by 1° and

the same translation process was repeated. Initial range of scanning was 180° for Hounsfield's design, completed in 5 minutes. Nowadays scanners can obtain views over 360° in less than 1 minute. [20]

Second Generation: First generation CT results were promising, but the acquisition time had to be reduced. This reduction was achieved by adding more narrow beams and detectors, as well as increasing the scanning time by 1/N, N being the number of detectors. However, after 20 beams and detectors, the improvement was limited with the physical complexity and geometry [20].

Third Generation: In order to decrease the scanning time further, a broad fan beam was used instead of a narrow X-ray beam, which widened the range of the beam to cover the whole patient. Tube and an array of tightly packed detectors were attached together to rotate at the same speed (rotation-rotation motion). Number of detectors varied from 250 to 750 in order to allow enough measurements across the scan circle. An example of the fan beam geometry compared with conventional parallel beam geometry is previously shown in Figure 2.2. [21]

With the 3rd generation, hundreds of image projections could be obtained during less than 10 seconds of scanning time [21]. However, this generation of scanners needed a high stability of detectors and matching of detector responses. Any detector error or drift in the calibration was also transferred to the image as "ring artifacts." If one of the detectors is out of calibration Figure 2.9, detector will give erroneous values at each reading, leading to a circular shift [22].

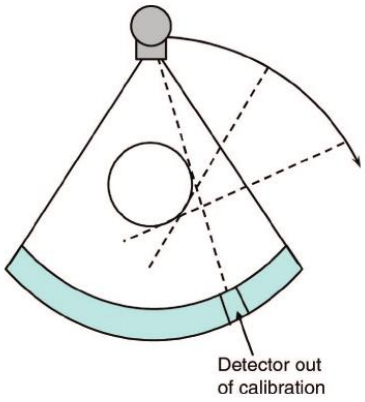

Figure 2.9: Formation of ring artifacts due to the detectors. In the figure, the detectors that are out-of calibration create a circular shift at each reading [22].

As a solution for the ring artifacts, xenon detector arrays were introduced, where a long chamber of xenon array was divided into smaller chambers by thin plates called septa, which provided an improved stability and well matching since whole array was affected in the same way by the external factors. However, the ring artifacts introduced by the 3rd generation CTs were never completely eliminated, only diminished by high-quality detector design and frequent calibration scans. [20]

Fourth Generation: Fourth generation geometry was developed with the support of National Institutes of Health in 1976. Difference between 3rd and 4th generations is

shown in Figure 2.10. Unlike 3rd generation CTs, where both detector and X-ray tube rotated separately, 4th generation detectors were placed on a 360° stationary array in these CTs, enabling them to detect rays at any distance from the center of rotation.

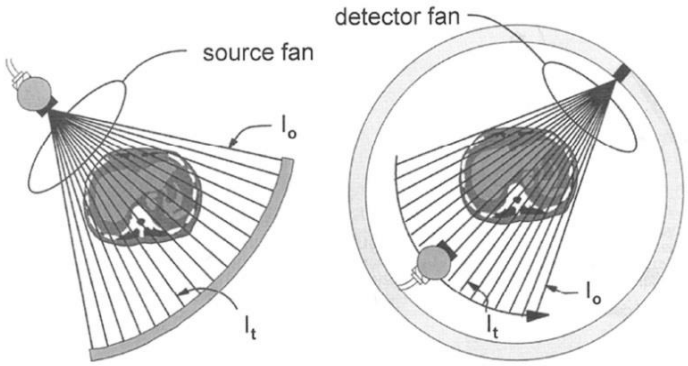

(a) (b)

Figure 2.10: (a) 3rd generation and (b) 4th generation CTs. In 3rd generation CT, detector and X-ray tube rotate separately, which can cause calibration errors. In the 4th generation, this risk of calibration error is corrected by placing the detectors on a 360° stationary array [23].

Also in the 4th generation, ring artifacts generated by patient shadowing were compensated with dynamic calibration of the detectors. Some of the main disadvantages of this design were the large ring diameter (1.7-1.8 meters), which was necessary for acceptable tube-skin distances and compensation of increased scatter. Use of the scatter absorbing septa, which was used in 3rd generation CTs, was not feasible for the design of this generation because septa would aim for the center (patients location), leading to transmission of primary X-rays. Both 3rd and 4th generation CTs were produced until the recent development of multislice CTs, which eventually replaced the 4th generation models due to their lower cost than the expensive detector arrays used in the 4th generation technology. [20]

2.4. Dental Computed Tomography

Study of Gahleitner *et al.* provides a useful overview about the concept of dental CT and the history behind this technology. In their work, dental CT is referred to as a specific investigation protocol rather than a certain imaging modality, which includes extremely accurate acquisition of axial jaw scans.

Dental CT, also known as Dentascan, was introduced by Schwarz *et al.* in 1987, where they used the first curved multiplanar reconstructions of the jaw. This reconstruction has become a common method prior to metal implant surgeries and its clinical use has increased over the past 20 years. The primary motivation for dental CT was the increased number of metal implants in the jaw and the need for imaging the jaw anatomy despite these implants. Major disadvantage of X-ray CT was the metal artifacts caused by tooth fillings in the jaw region, and this problem was overcome in dental CTs by using axial plane instead of the coronal plane for scanning, leaving the artifacts on

occlusion plane and the jaw undistorted, thus enabling the dentists to accurately visualize the actual jaw size [2]. Dental CT is currently used in areas such as analysis of jaw pathology, assessment of impacted teeth, supernumerary teeth and their relation to vital structures, changes in cortical and the assessment of bone grafts, examination of paranasal sinuses, and obstructive sleep apnea [24].

Dental panoramic X-ray: Until 1987, radiographs were sufficient for dental imaging industry. However, after the introduction of dental CT, reformatting programs for dental imaging increased and spread around the world. The main reason for that were dental implants, which were metallic cylinders, surgically implanted into the jaw in order to provide support for a dental prosthesis. With the metal artifacts caused by these implants, it was difficult to determine if there was enough bone in the jaw to place the implants. Also dentists could not detect the exact location of the soft tissue and nerves. With the development of dental CT, new methods for evaluation of dental implants were developed, as well as improved assessment of the tumors, silicon implants, fractures and inflammatory diseases [25]. Nowadays dental panoramic X-rays are used in examination of radicular lesions, radicular granuloma, dental fillings extrusion, calcifications, demineralization, bone lesions, included tooth [26].

3. CONE BEAM COMPUTED TOMOGRAPHY

Starting from the early days of dental radiographs, concepts in imaging technology did not change significantly until 3D imaging. First CTs suitable for 3D imaging were available since 1980s, but they were expansive, the access to the technology was limited, radiation dose was high, and their utilization was limited to unique dental problems. Therefore 3D imaging was not commonly used until 1988, when the first spiral and helical scanning was introduced [27].

One of the last generations of 3D imaging modalities is Cone Beam Computed Tomography (CBCT), which provides a high quality and accurate 3D representation of a subject. It is preferred over other CT types due to its small field of view (FOV) and low dose radiation with sufficient image spatial resolution [28]. Examples of commercial CBCT units are presented in Figure 3.1.

Figure 3.1: Examples of hybrid CBCT units. (a) KODAK Dental Imaging 9000 3D, (b) Veraviewepocs 3D, and (c) Picasso Trio [28].

Layman *et al.* describes CBCT as a more compact, faster and safer version of conventional X-ray CT [29]. CBCT was firstly used as a prototype in clinical practice as early as 1982 for angiographic applications [30]. However it was introduced in dento-maxillofacial (DMF) imaging in 1997 and since then its clinical applications in dentistry has been numerous [27]. CBCT is becoming popular around the world especially for pre-operative assessment (before operation), intra-operative (during operation) and post-operative (after operation) imaging in dental surgeries [28]. It has been also validated for biomechanical simulations, models of bone remodeling and simulations for orthodontic assessment, treatment, and follow-up [31]. Number of CBCT units used for maxillofacial imaging has been increasing [32], and the 19 different commercially available CBCTs around the world as of this writing, are listed in the Appendix 1 [28].

3.1. Limits of 2D Imaging

2D imaging has been used in dentistry since the first intra-oral radiograph was taken in 1896 [24]. Ii is known that in 2D imaging, the acquired image is a 2D representation of a 3D object. In case of any corruption or error in the imaging process most probably that lead exposure or geometric errors, and the result would be far from optimal. Moreover, complex dental anatomy and closeness of the surrounding structure can also “shadow” the accurate representation of the 3D image in 2D slices. None of the 2D imaging

techniques, i.e. intraoral, panoramic and cephalometric images, is able to demonstrate the 3D anatomic features in the same way as CBCT because CBCT reconstructs the projection data to provide interrelational images in axial, coronal and sagittal planes. Conventional CTs captured the axial plane slices as separate stacked slices or from a continuous spiral motion over the axial plane with several rotations. However, CBCT uses only one or two rotation sweeps and data acquisition can be obtained from a limited region or whole dental/maxillofacial volume [33]. Also data can be re-organized in their true relationships via CBCT, which cannot be accomplished with 2D imaging. [28]

3.2. Cone Beam Computed Tomography Principles

CBCT technology was essentially innovated as a cost efficient method for obtaining 3D cross-sectional images for radiotherapy. CBCT is based on the principle of rotating a scanning unit (gantry), which is fixed to an X-ray source and detector (Image Intensifier or Flat Panel Detector) [34]. The X-ray beam is characterized with different parameters: (1) beam quality, defined by the X-ray spectrum, (2) shape of the beam, defined by the voltage peak (kVp) over the X-ray tube, the anode current and the filtration of the produced X-ray beam [34]. CBCT uses a pyramid or cone shaped ionizing radiation source, which is produced in the X-ray tube. This cone shaped source transmits the X-rays through the middle of the region of interest (ROI) onto the detector on the opposite side of the patient. Whole field of view (FOV) is scanned by the detector and X-ray source, which rotate with a constant fulcrum, scanning a range from 180° to 360 ° [28]. The smallest 3D unit obtained from the FOV is called a voxel, which are stacked in rows and columns. Information such as dimension, 3D location and value for each voxel are stored in the computer [33].

Operating range of CBCT can be as low as 1-15 mA at 90-120 kVp from the range of 120 – 150 mA at 220 kVp of CT. Radiation dose used in CBCT depends on the scanning time. So if the scanning time is considered to be typically between 5.7 to 40 seconds, then the exposure is in the range of 40 to 135 microSievert (μSV), whereas this value is around 430 μSV for a multi-slice CT [31], [35]. The radiation dose of CBCT can be 3 to 7 times more than panaromic doses, whereas it is around 40 % less than conventional CTs [31]. However, the effective dose of CBCT can change depending on the size of FOV, mA setting, kVp, scan time, sensor sensitivity and number of image captures. [35]

3.3. Limitations of CBCT

Although new CBCT technologies enabled dental imaging with low radiation exposure, high resolution and decreased expenses, it has several important drawbacks such as susceptibility to movement artifacts, low contrast resolution and limited capability to visualize internal soft tissues [24]. Figure 3.2 indicates the lack of contrast in the soft tissues of maxilla region in CBCT compared with a Medical CT (MDCT).

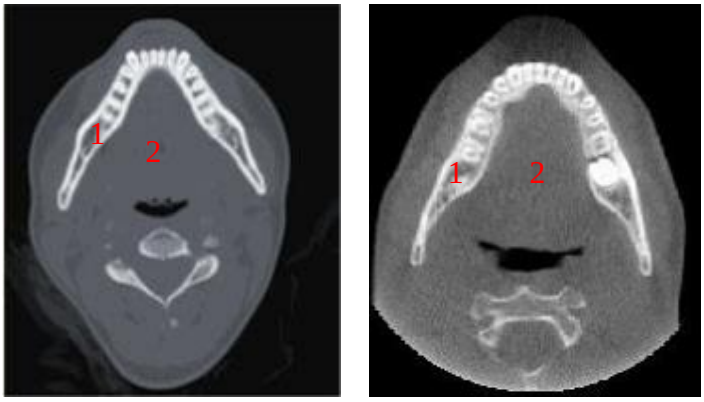

(a) (b)

Figure 3.2: (a) Medical CT (MDCT) axial image (b) CBCT axial image (upper jaw) showing hard (1) and soft (2) tissues of maxilla. The low contrast of high density objects in the CBCT image is clear when compared with the MDCT structures [Modified from [36]].

Even though movement can be prevented, low contrast and limited capacity of visualization in CBCT are issues related to the Hounsfield Units (HU), which need to be solved. Unfortunately, as opposed to medical CTs, CBCT technology does not allow an accurate identification of HUs of the anatomical structures. This is mainly because of the fact that CBCT manufacturers have not agreed on a standard scaling system for gray levels representing the attenuation coefficients. The problem of non-standardized HU scale is explained in the study of Esmaili *et al.*, where they compare two commercial CBCTs. In their study, it was observed that Planmeca Promax X-ray machine produced more severe artifacts due to the lower radiation dosage (84 kVp vs. 110 kVp) its limited tilting capacity (270° vs. 360°) and the type of the software used in the device, whereas NewTom VG resulted in less artifacts for the same configuration [37]. Different and inaccurate HU values in the study can also be explained by increased scatter and beam hardening affects. Nevertheless, these problems prevent the use of CBCT for bone density estimation applications [38]. Furthermore, lower energy (in kVp) of the X-ray beams in CBCT makes the reconstruction more prone to metal artifacts [30]. Additionally, due to the novelty of cone-beam technology, little research has been conducted on how to apply the artifact reduction techniques developed for CT to CBCT images.

4. ARTIFACTS CAUSED BY METALS IN X-RAY COMPUTED TOMOGRAPHY

One of the major problems in X-ray CT technologies is the artifacts caused by metals. Since CT images are comprised of many independent detector measurements, the measurement system is highly sensitive to distortions, thus it is inherently more prone to artifacts from several sources, especially high density materials such as metals. Artifacts in X-ray CT, originating from metals, are discussed in this section.

4.1. Metal Artifacts in X-ray CT

When X-rays reach a metal in the body, they are attenuated significantly, causing fewer photons to reach detectors. The nonlinearity caused by low photon count produces corruptions, seriously deteriorating the image quality near the metal surfaces and causing the phenomena explained in this chapter [1]. Artifacts originating by metals include beam hardening, non-linear partial volume effect, exponential edge gradient effect (EEGE) and scatter; and they are likely to compound the problem with very dense objects [39]. For instance, beam hardening causes attenuation of the photon energies during the acquisition of the projection data and leads to artifacts around the metals. Using less attenuating materials such as titanium could decrease the X-ray attenuation, however dental materials are not mainly chosen based on the X-ray attenuation properties. Therefore material removal is not clinically practical in the case of dental CT imaging [5]. Another solution could be increasing X-ray energies to improve photon penetration because higher dosage of radioactivity would significantly increase the imaging quality. However, radiation dose for dental patients needs to be optimized in order to achieve the lowest practical level in clinical applications in accordance with the principal of "as-low-as-reasonably-achievable" (ALARA) [40].

In order to apply a successful metal artifact reduction (MAR), it is important to understand the physical phenomena caused by metals in dental X-ray CT images. In this section, some of the most common sources of artifacts caused by metals are investigated. It should be noted that, although there are other sources of artifacts including aliasing, motion, detector under-sampling and range exceeding, they have minor affect in the case of X-ray CT reconstruction [5]. Therefore, they are not considered in the scope of this thesis.

4.1.1. Beam Hardening

When a polychromatic X-ray (an X-ray beam consisting of photons within a wide energy range) passes through an object, the attenuation of the rays increases as the energy decreases. Linear attenuation coefficient (μ) is used as a measure of attenuation, and it is greatly dependent on the photon energy. The higher the photon energy, the lower is μ, which means that low energy components are attenuated more than the high energy photons. Attenuation of low energy rays increases the energy of the beam, making it "harder". Ideally, image reconstruction techniques assume linearity between the thickness of the object and the measured photon count. However, due to this hardening affect, the attenuation (photon count) and absorber thickness (path length

traveled by the beam) cannot be considered as linear anymore. Rays that travel a shorter distance in the object are less attenuated, causing less errors in the measurements whereas the ones that travel a long distance are highly attenuated, leading to greater error values [11]. When CT image is reconstructed with these errors, it causes black and white streaks as demonstrated in Figure 4.1. The dark streaks in Figure 4.1 indicate the direction of the highest attenuation.

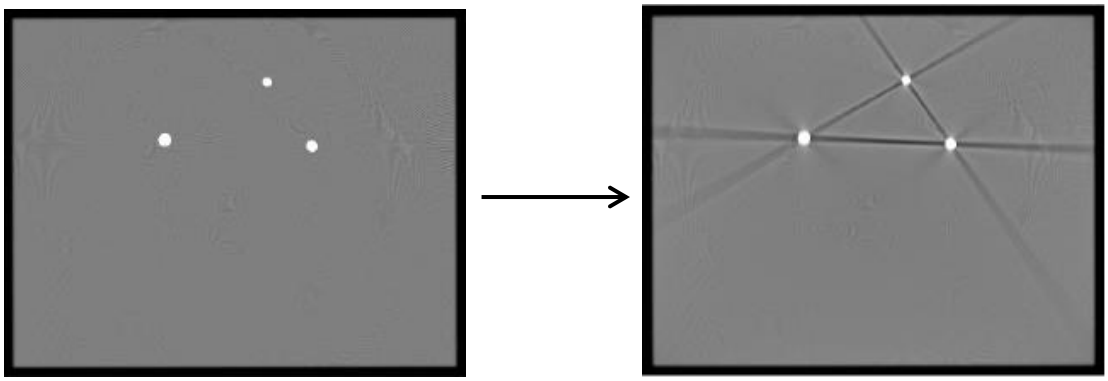

Figure 4.1: Phantom of a plexi plate with 3 amalgam fillings (left) without beam hardening (right) with beam hardening [11].

It can be said that in Figure 4.1.b, amalgam fillings cause beam hardening because they behave like a filter for X-rays. Fillings highly absorb/filter the low-energy beams, and lead to larger intensity values in the place of the metal, shadowing the intensity values of the matter behind the metal in the beam path [41]. This absorption and shadowing generate the streak artifacts in Figure 4.1.

4.1.2. Scatter

Many photons diffract from their original direction when they penetrate through an object. Due to this deviation they cannot be used in the calculation of accurate directional information in reconstruction. Even though most of these deviated photons are eliminated by post-patient collimation and septa between two detectors, some of them still contaminate the measurement [11]. Similar to beam hardening, scatter also causes nonlinear behavior of the beams, resulting in projection errors, and causing similar artifacts in the images [11]. Figure 4.2 shows amalgam fillings causing dark streak effects in the direction of highest scatter.

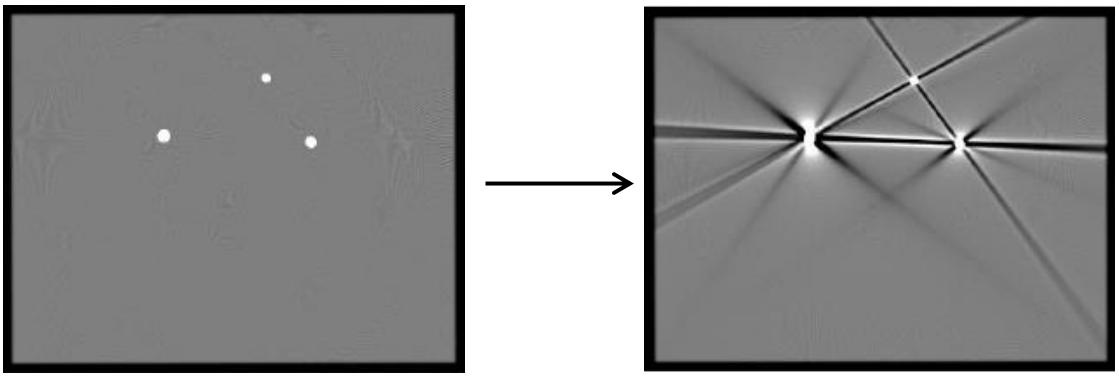

Figure 4.2: Phantom of a plexi plate with 3 amalgam fillings (left) without scatter (right) with scatter [11].

Scattered photons increase the intensity value of the primary intensity I_0, causing overestimated intensities along the ray path, thus, leading to streak artifacts after reconstruction [41]. In order to decrease the effect of scatter, perfectly collimated detectors are needed. Also scatter correction can be used for reducing the artifacts, but a constant scatter over the entire projection is assumed for this correction [10]. Considering the fact that larger detectors in CBCT detect more scattered photons, it can be said that CBCT is more vulnerable to scatter than conventional CTs [41].

4.1.3. Noise in Measurements

There are two types of noise in CT. One of them is caused by the quantum nature of the X-ray photons, modeled by the Poisson distribution. Noise can be decreased by either increasing the X-ray exposure to the patient or by increasing the voxel size, at the expense of decreasing the spatial resolution. The deviations and fluctuations in the measurements cause dark and bright streak artifacts along the projection lines after reconstruction. As it is shown in Figure 4.3, streaks are more apparent in the direction of higher attenuation, because low intensity of the measured data leads to a lower signal-to-noise (SNR) ratio, making the noise more dominant over the measured intensities.

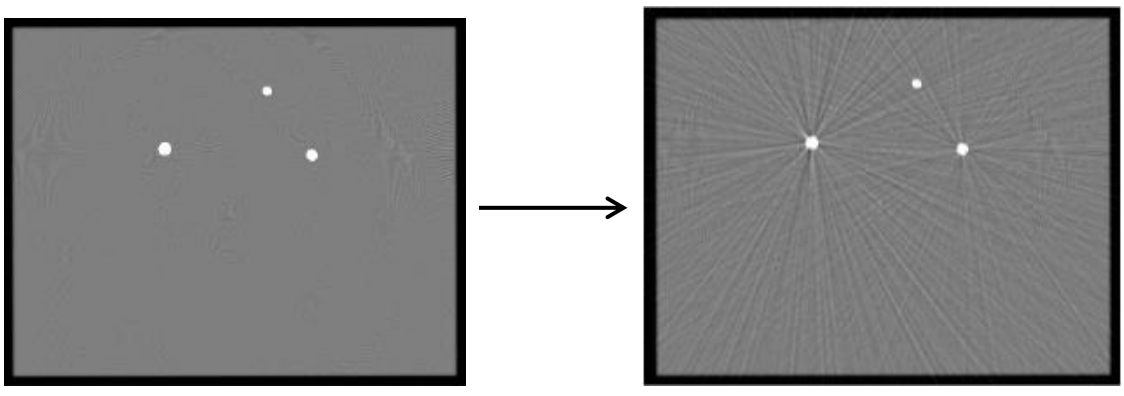

Figure 4.3: Phantom of a plexi plate with 3 amalgam fillings (left) without noise (right) with noise [11].

Other type of noise is the CT measurement system, which is a combination of different noise sources such as the exposure time, beam energy, tube current, phantom size, collimation/reconstructed slice thickness and helical pitch [42].

Post processing of the images by averaging is the most efficient way to decrease the effect of noise in the images, since the consistent structures cumulatively dominate during the repetitive averaging, whereas the noise is either minimized or cancelled out. As a drawback, averaging operation causes blurring in the image by smoothening the edges of the objects.

In the case of CBCT, the average dose of radiation is much lower than in conventional X-ray CT. Therefore, noise alters the attenuation values of voxels more, where they need to be constant. These altered values change the computed attenuation values of tissues, leading to errors in the backprojection process and causing lower SNR (low signal, high noise) ratios in the measurements [41].

4.1.4. Exponential Edge-Gradient Effect

Exponential edge gradient effect (EEGE) often occurs in case of high contrast differences between neighboring structures, where there is a sharp “edge” between the high and low density objects. In CT measurements, sharp intensity changes are considered as high frequency components. Although in theory these high frequency components (edges) are considered as lines, in practice these lines are averaged in a finite line width, leading to smoothening (blurring) of the edges up to a certain degree [43]. Especially in dental imaging, due to the high contrast difference between the metallic crown borders or the edges between bone and soft tissue, EEGE is a problem that has to be taken under consideration during image reconstruction [41]. In order to reduce the effect of EEGE, high pass algorithms are used to mathematically enhance the edges of structures and decrease the blurring effect [43].

4.2. Metal Artifacts in Dental Applications

In order to understand the effects of metals in dental CT, it is important to explore the anatomy of jaw in dental images. Figure 4.4 demonstrates the structure of an upper jaw (maxilla) without metals on a sample dental CT. Regions indicated with numbers 1, 2 and 3 in Figure 4.4 commonly correspond to HU values of ~2000, ~200, ~1200-1800 respectively [44].

(a) (b)

Figure 4.4: (a) CT of axial slice of maxilla, (b) 3D anatomical view of dental CT (CBCT) reconstructed from (a) with sections of 1 (tooth), 2 (soft tissue), 3 (jaw bone). All structures are clearly visible with no metals. [Modified from [45]].

Metals that are present in dental CT images introduce strong artifacts where two metals meet or overpass in scan rotation [1]. These metal artifacts in CT images have relatively high intensity values (amalgam and gold have attenuation values greater than 30,700 HU), and they prevent precise 2D visualization, hinder structures and distort the 3D reconstruction [44]. Figure 4.5 demonstrates metal artifacts caused by beam hardening, scatter and EEGE, which hinder the structure of nearby teeth as well as the soft tissue. It is also worth noting that black and white streaks in Figure 4.5 are amplified as the metals get closer to each other. Also filtering operation during FBP causes additional streak artifacts on the image, especially when the FOV is small and includes multiple metals.

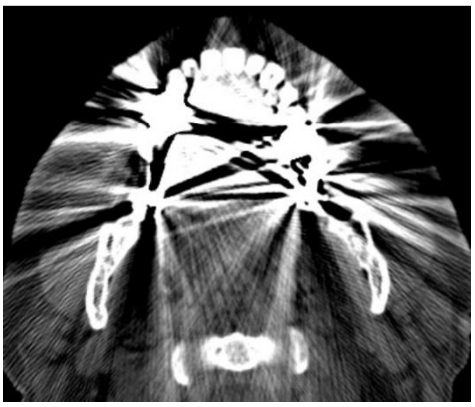

Figure 4.5: Metal artifacts in dental CT of maxilla after FBP (axial view). Anatomical structures are shadowed and distorted by the metal artifacts [46].

In dentistry applications, accurate information about the 3D structures of teeth and maxilla for diagnosis and planning of dental surgery is needed. It is worth noting that importance of the metal object extraction is not limited to MAR in CT images. Detecting metal objects in dental CTs is also useful for sparse projection data. It can be

used in practical applications such as dose reconstruction in brachy-therapy and seed implantation [47].

Aforementioned artifacts are identified and compansated with MAR, which includes mainly categorized 4 parts: (1) Construction of sinograms (RT), (2) segmentation of the metals in the sinograms, (3) compensation of the sinograms for metal artifacts (MAR), (4) post-processing (FBP) of sinogram data. These steps are shown in Figure 4.6.

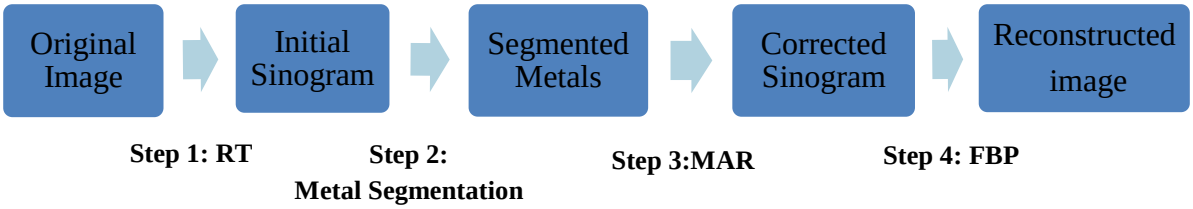

Figure 4.6: Block diagram comprising the steps of a MAR method

This thesis primarily compares two MAR algorithms on simulated and experimental datasets, aiming to achieve the best reconstruction with minimum error at the sites around the metallic parts. Both MAR methods are applied to the sinogram domain images, where all high density structures have a continuous imprint. Experimental dataset, obtained from Cone-beam Computed Tomography (CBCT), was only used for evaluating the performance of the developed MAR algorithms, whereas an additional jaw tilting in spatial domain was applied on the simulated 3D jaw phantom. The aim for jaw tilting was to decrease the coplanarity of metals in the source-detector plane, thus reducing the metal artifacts on each slice. Datasets and the jaw tilting operations are further explained in Chapter 5.

5. DATASETS AND EVALUATION METHODS

5.1. Simulated Dataset and Evaluation Methods

Phantoms are widely used for testing algorithms in medical imaging because real-life images include large amount of data, and phantoms decrease the processing time of the algorithm. Also it is highly probable for real images to include multiple sources of errors, which prevents accurate evaluation of the algorithm performance. Therefore, tilting of the jaw was implemented on a 3D jaw phantom in MATLAB (Windows version R2012b 64 bit), aiming to avoid the additional artifacts caused by X-ray CT systems.

5.1.1. Modeling of 3D Jaw Phantom

First step in modeling the jaw slices was to characterize the most significant parts in the jaw, based on their attenuation coefficients (intensity values). The most significant intensity characteristics were observed from oral cavity, bone, soft tissue, teeth and metallic regions, which led to the representation of these regions in the phantom. It should be noted that the structure of this phantom was modified from the 2D jaw phantom developed by Oliver Watzke [48].

Secondly, intensity values were assigned in such a way that gray level values of the anatomical structures would be proportional to their corresponding HUs in real CT images. Table 5.1 shows the selected intensity values for the anatomical compartments.

Table 5.1: Intensity values of modeled jaw regions

Modeled Region	Assigned Intensity Value
Soft tissue	0.5
Jaw bone	0.75
Teeth	1
Oral cavity	0
Metallic regions	10

In the construction of the phantom, the soft tissue surrounding the jaw was considered as the base. Two jaw bones were added on top of this base and then 32 teeth were placed (16 on maxilla and 16 on mandible).

Due to the structural similarity between upper (maxilla) and lower jaws (mandible), maxilla and mandible were constructed symmetrically. Once the 2D phantom was ready, it was modified so that maxilla and mandible would consist of 10 symmetrical slices. While modeling the maxilla and mandible, diameter of the crown was assumed to be constant, and teeth diameter was decreased towards the roots. Metallic regions were modeled with the same perimeter for each tooth, getting smaller in diameter towards the roots. The oral cavity was considered to be non-attenuating, thus it was modeled with 5 empty slices. The final 3D phantom had an axial size of 128x128 with 25 slices in total.

Figure 5.1 shows the 2D view of the jaw phantom for a single slice and its corresponding sinogram.

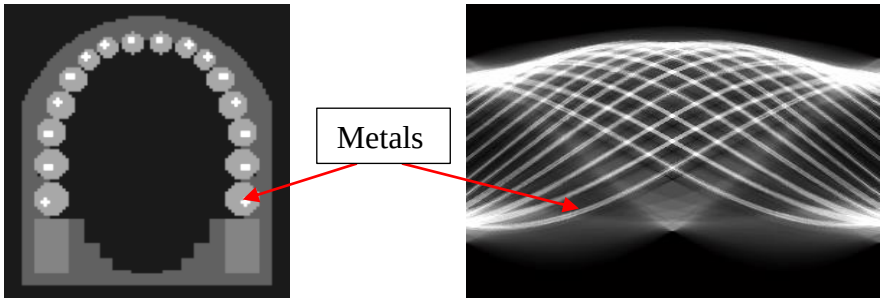

(a) (b)

Figure 5.1: (a) 2D view from 3D jaw slice with all of the metals (b) corresponding sinogram of (a). Metal traces on the sinogram can easily be distinguished from the rest of the anatomical structures due to its high intensity levels [Modified from [48]].

During the course of this thesis, Figure 5.1.a will be referred as the "ground truth", since its intensity values are known to be true, thus it can be used as reference in the evaluation of reconstructed images. Metals in Figure 5.1.b have significantly higher intensity values with respect to the surrounding area due to high intensity value accumulation from projection vectors of RT. This intensity difference, together with the continuous structure of the sinogram, makes it easier to segment these regions in sinogram domain compared to the spatial domain.

Jaw Tilting

In order to determine the tilting angles of the jaw phantom, the maximum angle was assumed to be 30° [49]. According to this maximum value, tilting was carried out in the range of [0, 30°], with an increment of 6°. For the computation of sinograms of tilted datasets, 288 projections were used in the range of [0,180°].

Since the tilting operation introduces new pixel values to be calculated, an interpolation technique is needed to estimate these values. In this thesis, nearest neighborhood method was selected for interpolation of the pixels. Nearest neighborhood method uses a linear approach for calculating the repositioned pixel values, which is represented with the formula of

$$y = y_0 + (y_1 - y_0) \times \frac{x - x_0}{x_1 - x_0} \qquad (13)$$

in the range of (x_0,x_1), where coordinates of two known pixel values are denoted by (x_0,y_0) and (x_1,y_1) , and y is the unknown value at location x [50]. This linear approach ensures that the interpolated values are as close as possible to the original values outside the metallic regions.

In order to investigate the effect of tilting in the source-detector plane on MAR, two tilting operations were carried out on the simulated dataset: (1) Tilting the jaw by angle α, corresponding to jaw opening/closing movement, (2) tilting the jaw by angle β,

representing the nodding movement. Figure 5.2 demonstrates the tilting with both α and β.

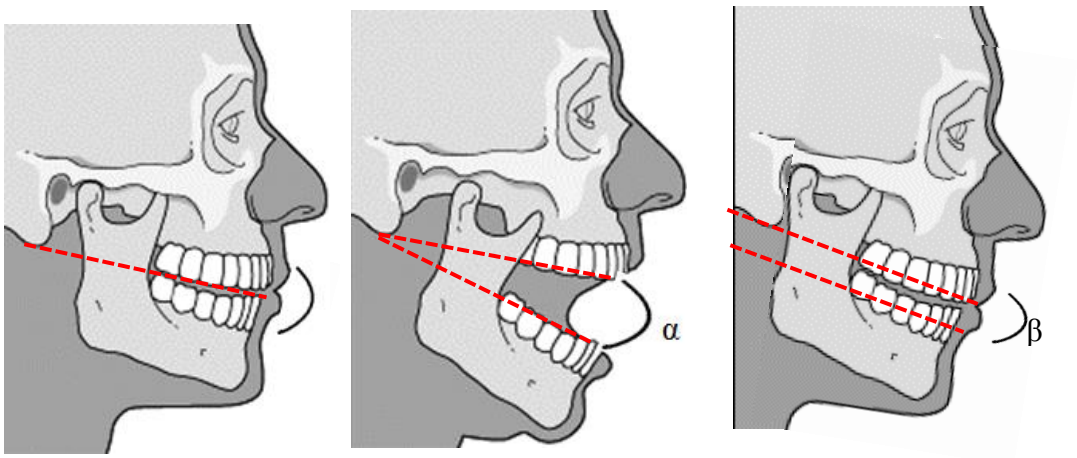

Figure 5.2: Coronal view of jaw with (a) no tilting, (b) tilting with α, (c) tilting with β. The dashed line in (a) indicates the original positioning of jaw, whereas dashed lines in (b) and (c) represent the amount of jaw tilt from (a) [Modified from [51]].

In the case of tilting with α, mandible and maxilla were tilted by α/2 degrees around the jaw joint, but in opposite directions. As degree of tilt was increased, metal amount per slice was lessened. Decrease of metals can also be seen from the comparison of Figure 5.3.a and Figure 5.3.d, where one of the three metals in Figure 5.3.a is almost invisible in Figure 5.3.d. Since the interpolation operation changes the size of the images, total slice number for α tilting was set to 110 from 25 by padding around the mandible and maxilla regions. Coronal views of the tilted jaw phantom are also provided in Figure 5.3.b and Figure 5.3.e in order to visualize the increase in the tilting angle.

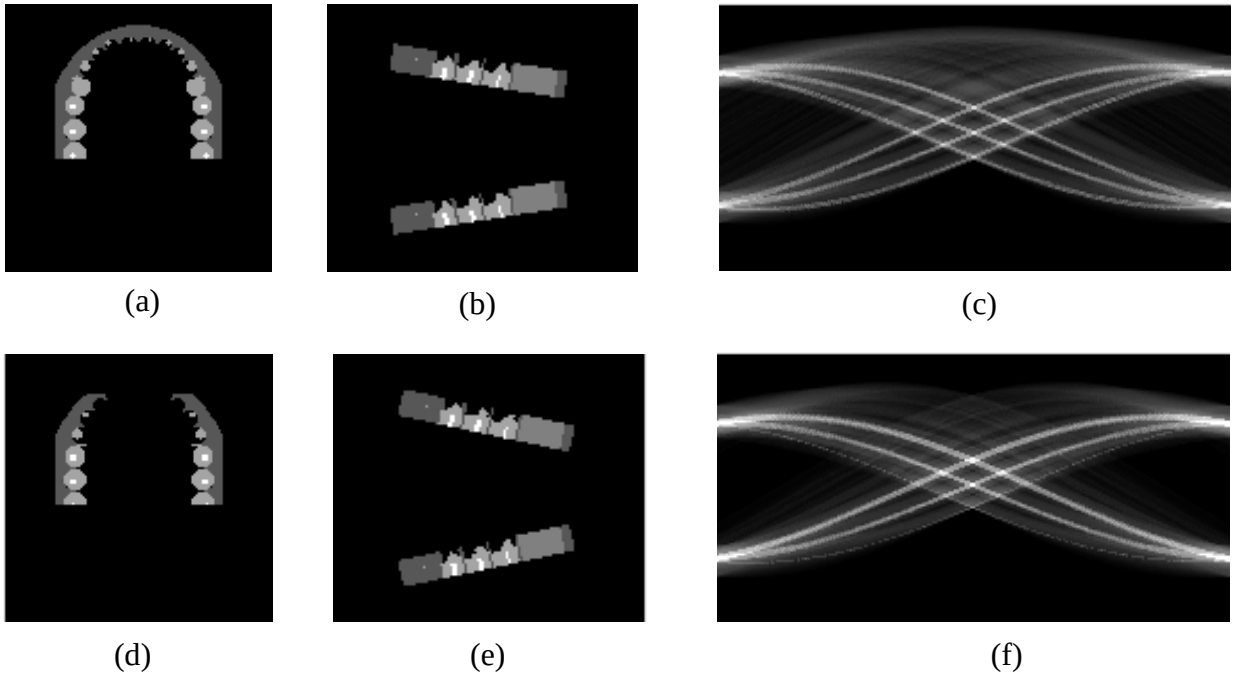

Figure 5.3: (a) Transaxial, (b) coronal, (c) sinogram views from 18° tilted jaw, (d) transaxial, (e) coronal, (f) sinogram views from α=24°. Transaxial views are used for demonstrating the decrease in metal numbers on the jaw slice, which can also be seen from the respective sinograms. Coronal view is used for visualization of the jaw movement.

In order to model the tilting by β, mandible and maxilla slices were tilted as a whole and in the same direction. An example tilt with β can be seen in Figure 5.4. When transaxial views in Figure 5.4.a and Figure 5.4.d are compared, it can be seen that as the tilting angle increases from 18° to 24°, visible area of the jaw on each slice decreases, simultaneously diminishing the metal traces to be replaced/ corrected in the respective sinograms from Figure 5.4.c to Figure 5.4.f.

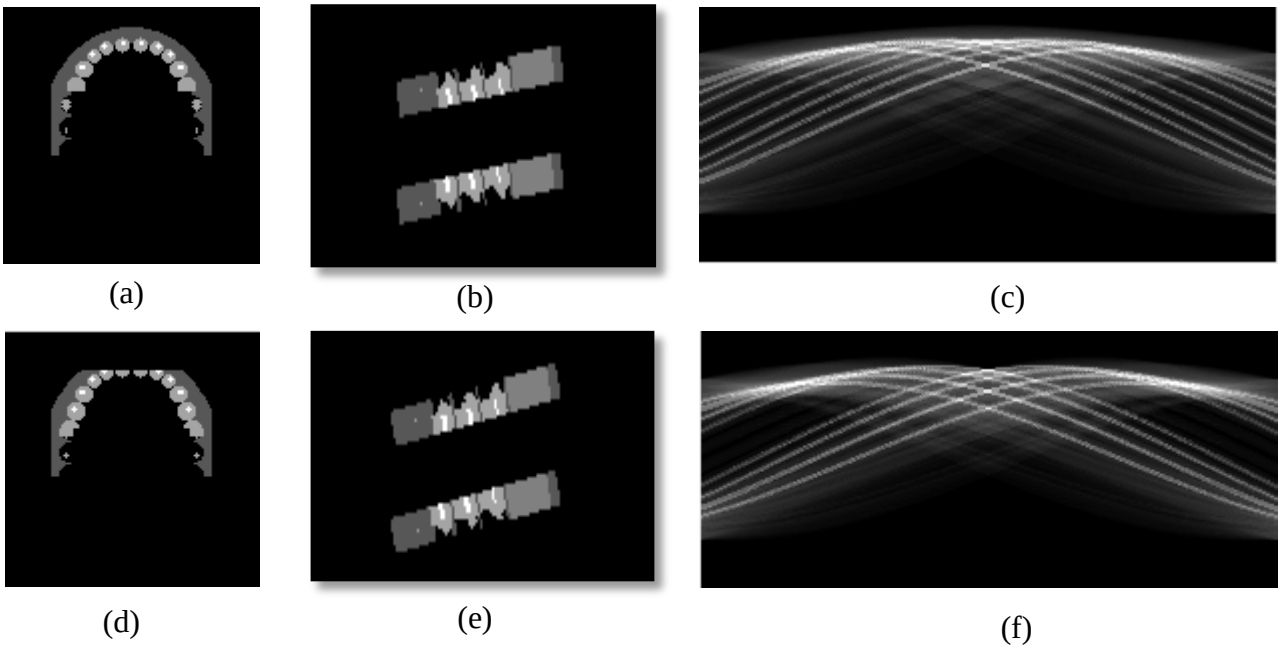

Figure 5.4: (a) Transaxial, (b) coronal, (c) sinogram slice views from β=18°, (d) transaxial, (e) coronal, (f) sinogram slice views from β=24°. Transaxial views and their respective sinograms are used for demonstrating the decrease in metal numbers on the jaw slice, whereas coronal view is used for visualization of the employed nodding movement.

In the case of β tilt, total slice number was set to 66. It should be noted that although the total slice number changed for different tilting techniques, axial image size for each slice remained the same (128x128) for both tilting alternatives.

5.1.2. Evaluation Methods

In order to evaluate the performance of the reconstruction for different tilting angles, 3D reconstructed images were tilted back to their original axes in spatial domain. Otherwise, same slice for differently tilted angles would have different amount of information, thus comparison between them would be impossible.

Line Profile Analysis

After all the 3D datasets were tilted back to their original axes, reconstruction quality between different tilting angles was compared with line profile analysis, which represents intensity (gray level) values along an arbitrary path on an image.

In this thesis, line profile analysis was used as a tool to compare the effect of tilting in reconstruction with respect to the ground truth image. A line, drawn on the image, was extracted from the rest of the values (Figure 5.5.b). Figure 5.5.a shows the polynomial line drawn on jaw phantom slice, which passes through the teeth and the background around the metal regions. Recalculated values of the metals are excluded from the line profile analysis since the most important part of MAR was the reduction of artifacts occurring around the metal regions rather than estimating the metal values accurately.

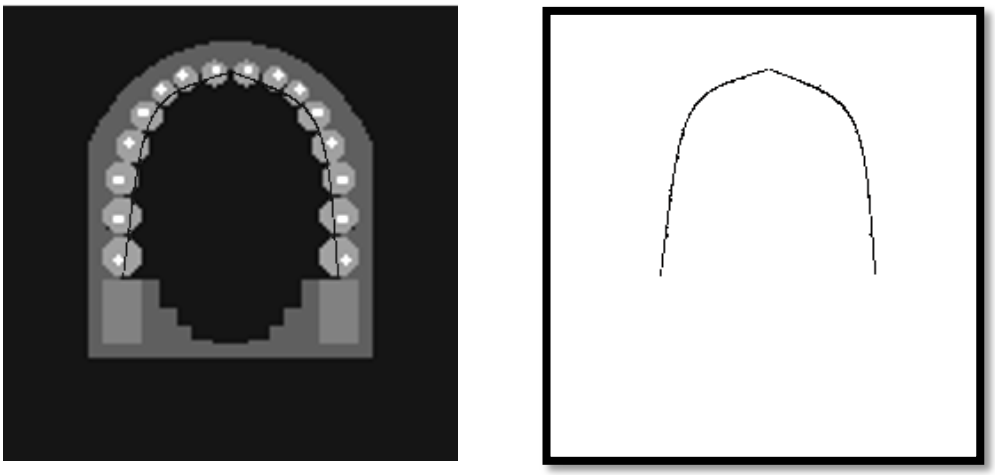

(a) (b)

Figure 5.5: (a) Ground truth image with the polynomial line and (b) line extracted from (a) for line profile analysis. Line is drawn on the ground truth so that it surpasses the jaw structures and the background, but excludes the metallic regions for obtaining a more reliable comparison between the reconstructed regions.

Once the line was drawn, intensity levels were determined at 170 sample locations on the line for 6 different tilting angles (0, 6°, 12°, 18º, 24°, 30°). Reconstructed images with different tilting angles were compared according to the intensity values on the line profiles.

Other image quality measurements

Normalized mean squared error (NMSE), peak signal-to-noise ratio (PSNR) and structural similarity (SSIM) index were utilized for further quantitative analysis of the simulated dataset. These quality measures were only used for the simulated dataset since they all require a ground truth reference for comparison. All of these techniques assess the similarity between two images, one of them being the ground truth image. For image quality assessment, NMSE and PSNR were calculated separately for reconstructed teeth, background and jaw regions, aiming to achieve a more accurate comparison in homogenous regions, decreasing the deviation in calculations. Selected regions quality measurements are shown in Figure 5.6.

(a) (b) (c)

Figure 5.6: (a) Segmented teeth, (b) segmented background, (c) segmented jaw regions used for image quality assessment. Note that the regions used in evaluation have the value of 1 whereas dark regions are 0.

Normalized MSE (NMSE): Mean squared error (MSE) describes the difference between intensity values of two images at coordinates of *(x,y).* MSE between ground truth image $g(x,y)$ and restored image $\hat{g}(x,y)$ is defined as

$$MSE = \left[\frac{1}{MN} \sum_{x=0}^{M-1} \sum_{y=0}^{N-1} \left[\hat{g}(x, y) - g(x, y) \right]^2 \right] \times 100 \quad (14)$$

where the image size is NxM and image values are normalized in the range of [0,1] [52]. NMSE is a scaled version of MSE, normalized in the range of [min(g (x,y)), max($\hat{g}$ (x,y))]. Minimum value of NMSE is zero, which occurs if $g(x,y)$ and $\hat{g}(x,y)$ are equal, and it indicates that there is no difference between the two images.

PSNR: Peak signal-to-noise ratio (PSNR) is defined as the ratio between the maximum power of the signal and the power of the corrupting noise. In this case, PSNR between ground truth image $g(x,y)$ and restored image $\hat{g}(x,y)$ is formulated as

$$PSNR = 10 \log_{10} \frac{\sum_{x=0}^{M-1} \sum_{y=0}^{N-1} \hat{g}(x, y)^2}{MSE} \quad (15)$$

where the numerator define the dynamic range of pixel intensities in an image of size NxM [52]. Maximum value of PSNR is infinity because of the division by MSE in (15), which has a minimum of 0.

SSIM index: Structural Similarity (SSIM) index measures the similarity between two images, where one of the images is assumed to be the ground truth, and the other image is considered to be the distorted image. SSIM index was developed by Wang *et al.*, and it has been a well-known image quality measurement method because it correlates with the quality perception of human visual system (HVS). Instead of adding up the errors in individual pixels like PSNR and MSE, SSIM index considers any image distortion as a combination of loss of correlation, luminance distortion and contrast distortion. In other words, error sensitivity approaches use perceived errors for image quality assessment, whereas SSIM considers image distortions as changes in structural information. SSIM index of 1 indicates a one-to-one match between two images. [53]

In the context of this thesis, SSIM index is only used as an additional measure along with PSNR and NMSE because of the small amount of structural change after MAR. The algorithm developed for MATLAB in [54] was utilized in the calculation of SSIM index.

5.2. Experimental Dataset and Evaluation Methods

In order to test the MAR algorithms on the experimental dataset, a sample sinogram slice was constructed from the provided 3D CBCT image, on which metal traces were mostly continuous. Different from the simulated dataset, additional segmentation methods were utilized in the experimental dataset in order to obtain a more accurate extraction of metals from the sinogram.

5.2.1. Reconstruction of Sinogram Data

For the construction of the sinogram data, a 16-bit full angle CBCT image, acquired from Planmeca Promax 3D Max CBCT (Planmeca OY, Helsinki, Finland) was used. The CBCT image had the axial size of 1472 x 1856, with 750 slices over 360 angles in total. For the images used in this thesis, scans were carried out with 60 kVp, with an exposure time of approximately 23 seconds, with 29 mA. Initial acquisition of the image was carried out by Romexis 2.3.1. Software (Planmeca OY, Helsinki, Finland) and saved in ".raw" format. Spatial image, provided by Planmeca, was constructed from projections by using Feldkamp-David-Kress (FDK) algorithm, which is a modified FBP used for reconstruction of images from cone beams. All parameters that were necessary for FDK algorithm was not provided for the experimental dataset, therefore a parallel beam approach was used in the construction of sinograms. Also later modifications on the sinogram were carried out in MATLAB environment since Romexis software was not available. In order to process the large amount of data, the axial size of the acquired image was downsampled to 736x368. Since pixel number and size were not as important as the intensity changes in the image, downsampling did not impair the MAR calculations. After the image was downsampled, each sinogram was constructed into the 750x368 matrix, where all axial slices taken from a certain angle were stacked together. The sinogram, which was used in this thesis, and its construction are demonstrated in Figure 5.7. Initially constructed sinogram had intensity values varying in the range of [424, 8941], 424 being the darkest and 8941 being the brightest regions. This sinogram was modified with some pre-processing steps, which are explained in Chapter 7.4, in order to make it suitable for the application of MAR algorithms.

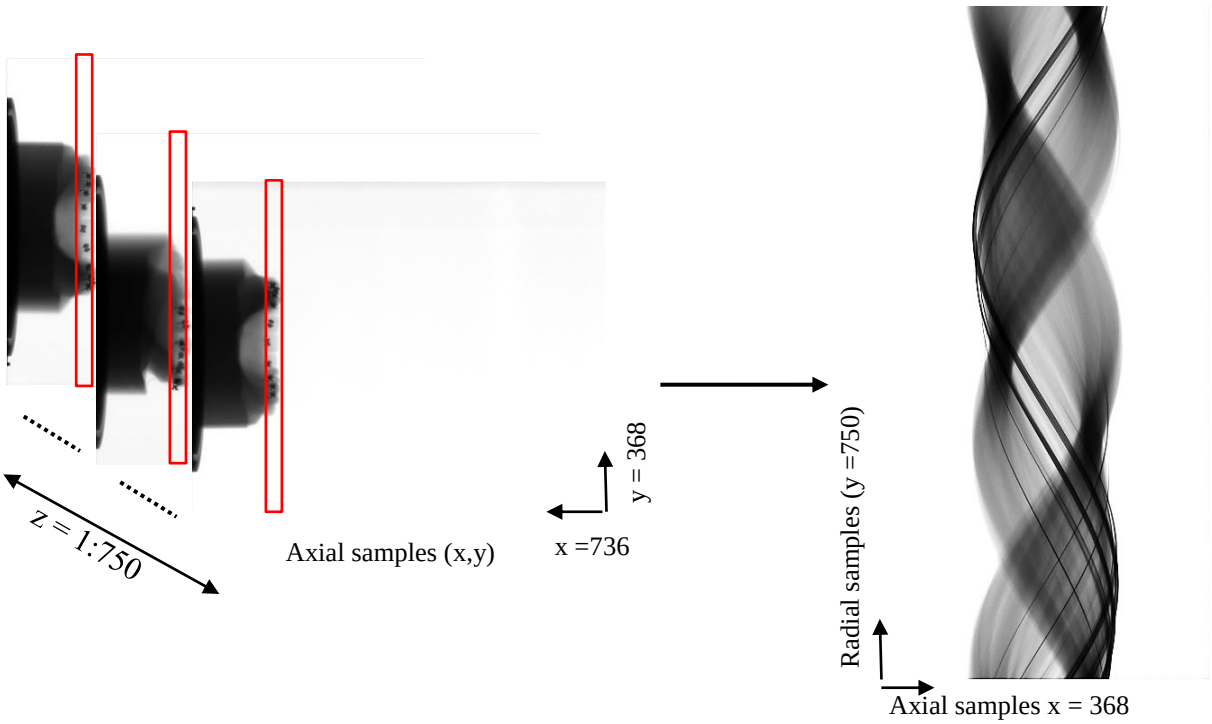

Figure 5.7: Sinogram construction from axial samples of the CBCT image. Marked regions from each axial slice of the CBCT data, consisting of all vertical values for a pixel, are stacked together. Resulting sinogram has the size of 368x750.

Final images after MAR were evaluated with respect to the jaw image depicted in Figure 5.8 (I_0). I_0 represents the spatial domain image with an axial size of 368x368, which was obtained after the application of FBP on the sinogram in Figure 5.7.

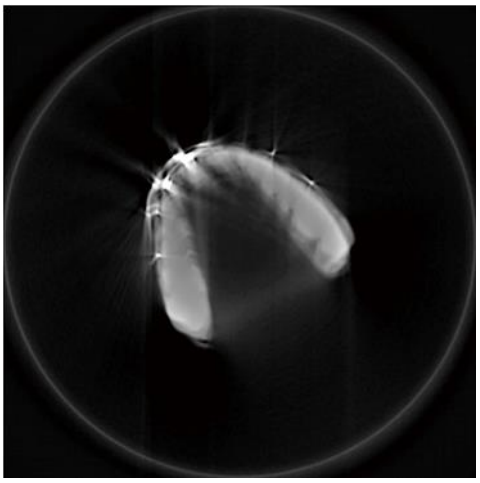

Figure 5.8: Jaw image in spatial domain, obtained after FBP on the original sinogram (I_0). It should be noted that pieces of the metallic braces have considerably higher intensity values compared to the other anatomical structures, thus, seem brighter in the image.

5.2.2. Evaluation Methods

Evaluation of segmentation and gap filling methods were initially assessed qualitatively. Since quality measures such as NMSE, PSNR and SSIM index could not be used due to the lack of ground truth information, mean values and standard deviations were calculated for sample ROIs. Chosen ROIs for evaluation are depicted on the uncorrected image in Figure 5.9.

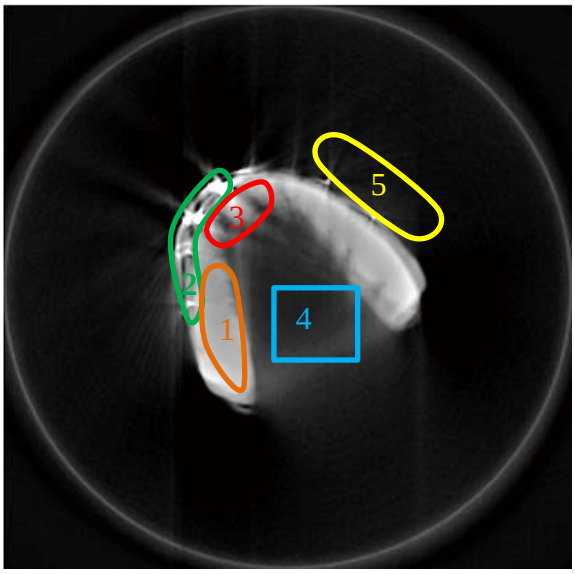

Figure 5.9: Selected ROIs on the uncorrected image. Marked regions are chosen as homogenous as possible within themselves, and are used for evaluating the reconstruction qualities of the MAR algorithms.

ROIs were selected so that each ROI would encircle a homogenous region or structure on the image. Standard deviation and mean values that were calculated in each region for the uncorrected image are presented in Table 8.3.

6. SEGMENTATION OF METALS IN DENTAL X-RAY COMPUTED TOMOGRAPHY

Most of the segmentation processes are based on the assumption that different kinds of materials have different CT value; and they can be detected by thresholding, above which a specific material/object can be separated from the rest of the image. Segmentation task would be trivial without the problems such as limited number of projection images, noise and artifacts in the projection data, and interpolation methods used in reconstruction algorithms [55]. In order to overcome these problems, there are different approaches to segmentation of high density objects such as (1) histogram based methods (*i.e.* Otsu's segmentation method [56] based on choosing a threshold according to the image histogram, or global thresholding), (2) region-growing approaches [57] and (3) watershed segmentation [58].

In the context of this thesis, finding the exact shape and location of the metals were the initial objectives in segmentation. It was important to detect the metallic regions as accurately as possible [59]. Any residual metals after segmentation would damage the reconstructed images, leading to streak artifacts, whereas over-segmentation of the metallic areas would distort the reconstruction quality of the non-metallic regions. Determination of the rest of the intensity distribution was not considered as a part of segmentation process, since they comprise completely different mathematical properties [47]. For segmentation, metal regions are considered as white (one) and non-metallic regions as black (zero).

6.1. Otsu's Thresholding Method

Otsu's Thresholding method was developed by Nobuyuki Otsu in 1979. It is commonly used in segmentation on sinogram data analysis. The method is based on the idea of choosing a threshold value from the histogram of the image, in which all the gray levels are grouped according to their occurrence frequency [56]. Once all the values are placed on the histogram, the gap between the peak values (representing objects) indicates the threshold to be selected. It is often difficult to choose this gap accurately due to several reasons such as noise and multiple peaks in the histogram. There are some sharpening techniques that can be applied on the histogram before selecting the threshold, but they mostly assume *a priori* information such as constant noise level and distribution. However, since *a priori* knowledge is often unavailable for medical images, these sharpening techniques are rarely applied.

Aim of Otsu's method is to provide a nonparametric and unsupervised method for histogram thresholding that would extract the objects of interest from the background. In this method, gray level that minimizes the weighted in-class variance is selected as the threshold value. The probability of two classes separated by a threshold t are represented with weights $\omega_{i,}$ and it is calculated as

$$w_1(t) = \sum_{0}^{t} p(i), \quad (16)$$

while the class mean $\mu_1(t)$ is found by

$$\mu_1(t) = \frac{\left[\sum_{0}^{t} p(i)x(i)\right]}{w_1}. \quad (17)$$

Together with (16) and (17), if the variances of these classes are represented with $\sigma_i^2(t)$ and the in-class variance with $\sigma_b^2(t)$, then $\sigma_b^2(t)$ can be written as

$$\sigma_b(t) = \sigma^2 - \sigma_w^2(t) = w_1(t)w_2(t)[\mu_1(t) - \mu_2(t)]^2. \quad (18)$$

Otsu's work shows that the threshold that minimizes in-class variance maximizes the between-class variance at the same time. The intra-class variances in (18) is defined as

$$\sigma_w{}^2(t) = w_1(t)\sigma_1{}^2(t) + w_2(t)\sigma_2{}^2(t). \quad (19)$$

Minimizing the in-class variance means making each cluster (object category) as tight as possible so that their overlapping is minimized. Tight clusters are achieved by simply calculating the mean value of each cluster and minimizing their variance. This algorithm provides a simple alternative to thresholding due to its computational simplicity. Since it is based on integration (global properties of the image) rather than differentiation (local properties in the image), it offers an automatic and stable solution to the selection of optimal threshold. [56]

6.2. K-means Clustering

In the clustering algorithms, objects with similar properties are grouped together in the same region (cluster). In image segmentation, it is assumed that objects with similar structures are in the same cluster, thus by minimizing the overlap between these clusters, a threshold can be selected. Clustering also uses aforementioned histogram approach similar to Otsu's thresholding. In order to find the appropriate threshold, following conditions needs to be satisfied:

$$\forall g \geq T : |g - \mu_B(T)| > |g - \mu_0(T)| \quad (20)$$

and

$$\forall g < T : |g - \mu_B(T)| < |g - \mu_0(T)|, \quad (21)$$

Where $\mu_B(T)$ is the average of four corner pixels that are assumed to be the background, whereas $\mu_0(T)$ is the average of all other pixels. Based on equations (20) and (21), threshold is placed in the middle of $\mu_B(T)$ and $\mu_0(T)$. Then these average values are updated by calculating the means of the pixels in each side of the selected threshold. Eventually, the algorithm converges to a final threshold, given that distributions have non-differing variances [60].

6.3. Segmentation of Metals in Simulated Dataset

Segmentation of metals in the simulated dataset was accomplished by Otsu's thresholding method. Steps of segmentation process are shown in Figure 6.1. It should be noted that some of the operations explained here are not shown among the segmentation steps in Figure 6.1 for the simplification of the diagram.

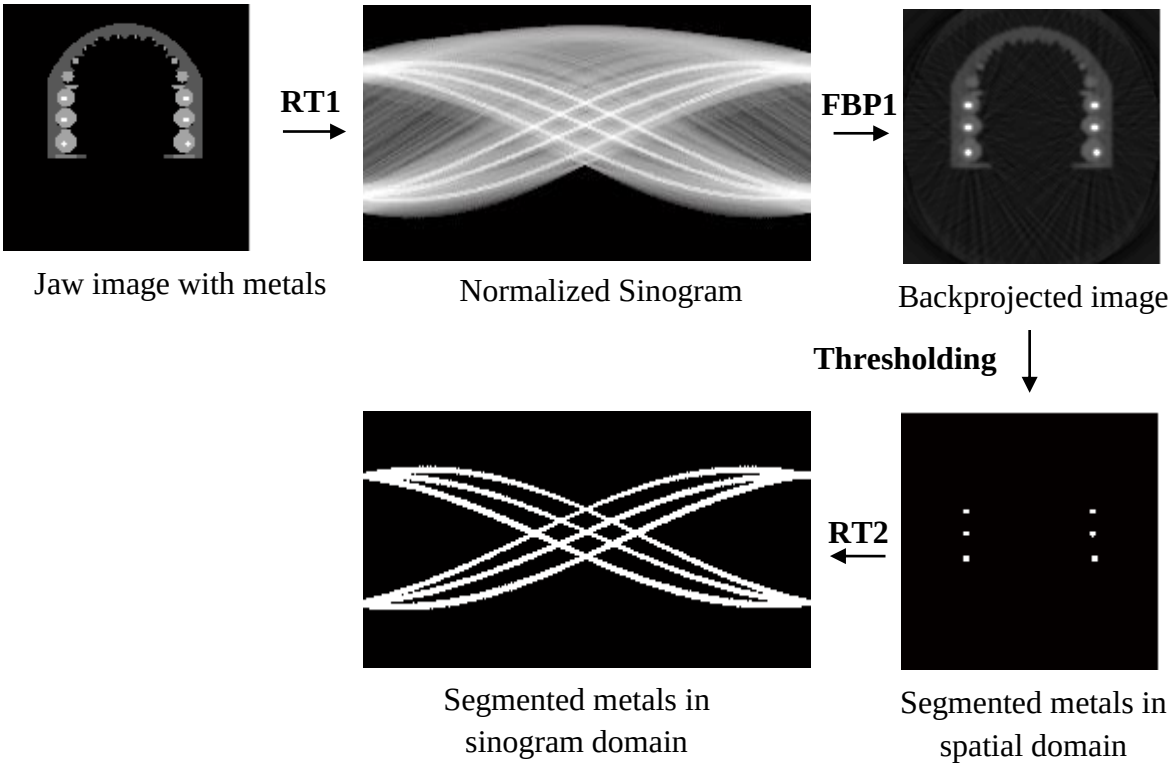

Figure 6.1: Segmentation steps for simulated dataset for β=18°.

In order to apply Otsu's method, simulated dataset was normalized between [0, 1] and transformed into sinogram domain (RT1 in Figure 6.1). Afterwards, edges in the sinogram were enhanced with logarithmic enhancement method. Mask obtained from Otsu's method was backprojected into spatial domain with FBP (FBP1 in Figure 6.1).

Later, metals were segmented by applying global thresholding on the backprojected image; resulting image was later transformed back to sinogram domain (RT2 in Figure 6.1). Finally, in order to obtain a better sinogram mask for MAR, sinogram of segmented metals was dilated for filling the discontinuities caused by thresholding operation. In order to improve the computational efficiency of the MAR algorithms, slices with metals were detected among the 3D stack and MAR algorithms were only carried out on those slices. Other slices with no metals were simply backprojected to spatial domain by using FBP.

6.4. Segmentation of Metals in Experimental Dataset

Segmentation of metals on the experimental dataset was accomplished by using three methods: (1) Otsu's thresholding, (2) logarithmic enhancement and (3) k-means clustering algorithms. The construction of the sinogram, on which segmentation was

applied, is further explained in section 5.2.1. In order to have a better visualization of the metals in the sinogram, intensity values on the original sinogram were reversed, making the metals brighter than the rest of the jaw. Then, gray level range was normalized in the range [0,1], where 1 (white) represented the brightest segments (metals) in the image, whereas 0 was used for the darkest regions. Resulting sinogram (S_1) is considered as the initial image for following segmentations steps. The sinogram masks, which were obtained after these segmentation methods, were later used to mask out the metallic regions on the original sinogram prior to the application of gap filling methods. Detailed segmentation steps are included in Appendix2.

6.4.1. Segmentation with Otsu's Thresholding Method

This method uses the intensity based segmentation of metals by using Otsu's thresholding algorithm. S_1 was used as the initial image for the algorithm, which is depicted in Figure 6.2.

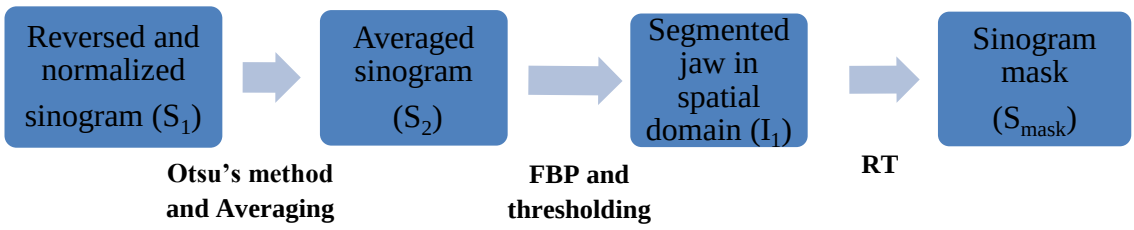

Figure 6.2: Block diagram for segmentation with Otsu's thresholding

Firstly, S_1 was thresholded by using Otsu's thresholding method. The obtained black and white sinogram was segmented again with different thresholds, which were selected around the Otsu's threshold. Resulting sinograms were averaged with different weights, aiming to make the metals more dominant in the sinogram compared to the rest of the information. Averaged sinogram (S_2) was backprojected to the spatial domain; resulting image was segmented by using simple global thresholding (I_1), which is depicted in Figure 6.3.a. After the last forward projection (RT), final sinogram mask shown in Figure 6.3.b was obtained (S_{mask}).

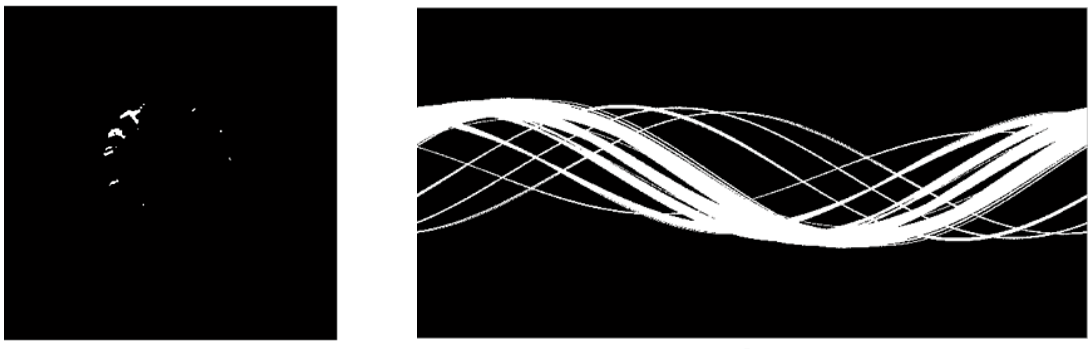

(a) (b)

Figure 6.3: Resulting image of segmented metals (a) in spatial domain (I_1), (b) in projection domain (S_{mask}) after Otsu's thresholding. Spatial domain mask in (a) is only used for visualization of segmented parts, whereas the respective binary sinogram in (b) is used for masking out the metals in MAR.

6.4.2. Segmentation with Logarithmic Enhancement

For the segmentation with logarithmic enhancement, logarithmic transform was carried out in addition to the pre-processing steps applied on the original sinogram. Block diagram provided in Figure 6.4 shows the segmentation steps used in this algorithm.

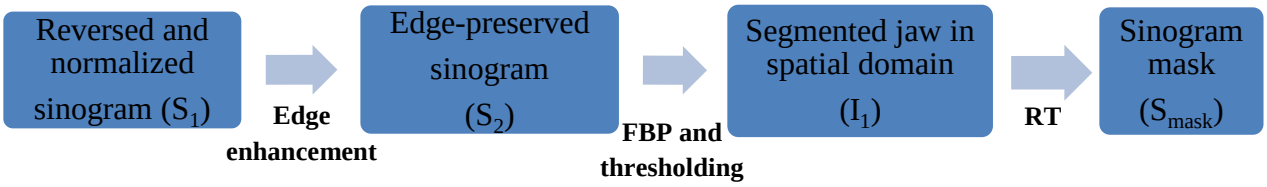

Figure 6.4: Block diagram for segmentation with logarithmic enhancement

Logarithmic transform was used to enhance the edges in the sinogram by mapping the darker (lower) gray level values into a wider range, whereas brighter (higher) gray level values are mapped into a smaller range. By using this edge-preserving transformation, difference between the metals and the jaw became more apparent on the sinogram (S_2), enabling a more accurate easier segmentation of higher intensity values. Afterwards, FBP and global thresholding were utilized for metal segmentation in spatial domain (I_1), providing a binary mask for metal values in spatial domain (Figure 6.5.a). In order to obtain the mask in sinogram domain, I_1 was transformed back into projection domain via RT. There were gaps on the sinogram, which were caused by the misclassification of some metal values after the thresholding operation. Final sinogram mask (S_{mask}) in Figure 6.5.b was achieved by filling these gaps in the metal regions.

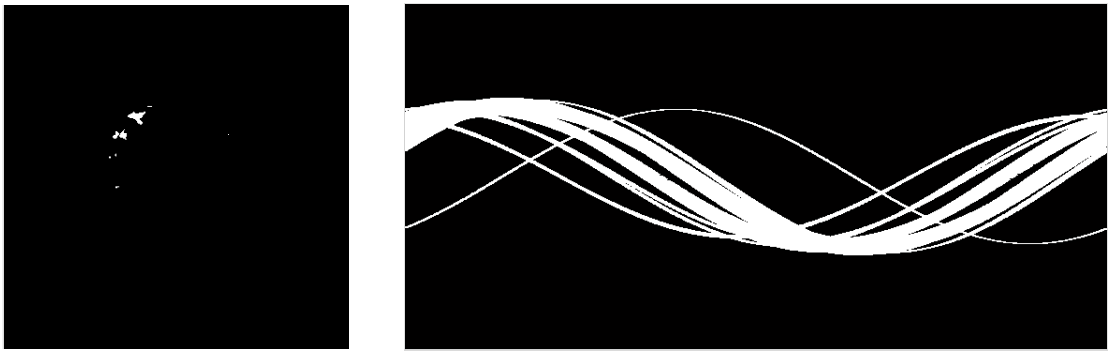

(a) (b)

Figure 6.5: Resulting image of segmented metals (a) in spatial domain (I_1), (b) in projection domain (S_{mask}) after segmentation with logarithmic enhancement. Spatial domain image in (a) only used for showing the positions of the segmented metals in the spatial domain image, whereas the sinogram mask in (b) is used in MAR.

6.4.3. Segmentation with K-means Clustering

Segmentation with k-means clustering can be considered as a combination of Otsu's thresholding and logarithmic enhancement methods, because it applies the Otsu's threshold on the edge preserved sinogram. K-means clustering algorithm later carried out with the thresholded sinogram in order to obtain a more accurate segmentation than

global thresholding. Steps of the developed k-means clustering algorithm are presented in Figure 6.6.

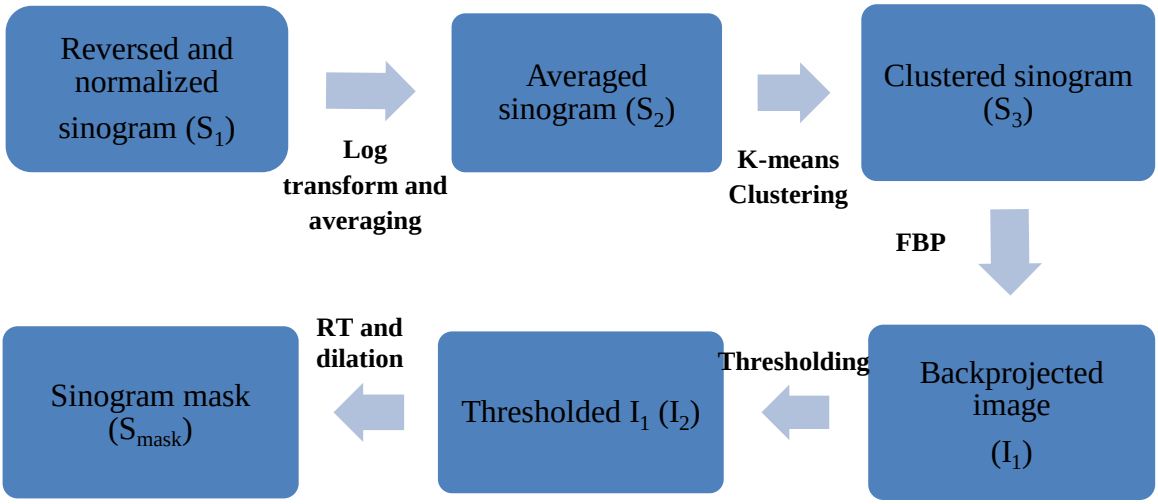

Figure 6.6: Block diagram for segmentation with k-means clustering

The averaged sinogram (S_2), which was obtained after log transform and averaging operations, was segmented into three clusters (metals, jaw and background), from which metal and jaw clusters were used to get an initial estimate for the FBP. This backprojected image was thresholded by 50% of its maximum intensity value (I_2), which segmented out the elements other than the metals. I_2 was transferred into projection domain with RT, and final sinogram mask (S_{mask}) was obtained after dilation operation. Spatial domain metal mask and finalized sinogram mask for this method are depicted in Figure 6.7.

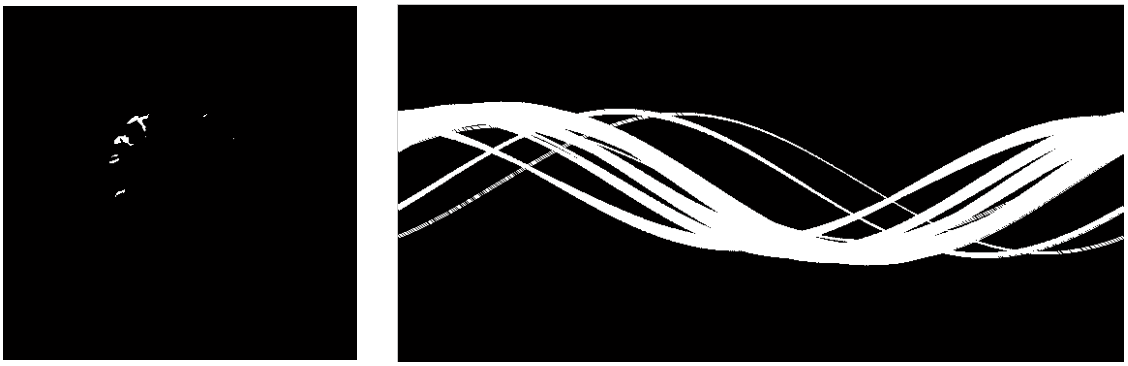

(a) (b)

Figure 6.7: Resulting image of segmented metals (a) in spatial domain (I_2), (b) in projection domain (S_{mask}) after segmentation with k-means clustering. Positions of the segmented metal objects are seen in (a), and sinogram mask in (b) is used in MAR.

7. METAL ARTIFACT REDUCTION TECHNIQUES

There are several MAR techniques, most of which consider the metal objects are considered as missing data [5]. These missing data parts are (1) recovered from the corrupted original data (Iterative reconstruction methods), (2) completely replaced by synthetic data on the sinograms (Projection completion/correction methods) or (3) corrected on projection data (Reconstruction correction methods) [61].

Projection completion/correction methods: Missing data are replaced by synthetic data, which can be obtained by polynomial or linear interpolation, pattern recognition or linear prediction method. Accuracy of these MAR methods mainly depends on tha accuracy of the metal segmentation. Considering the fact that metal artifacts consist of mixture of several artifacts, it can be difficult to detect the exact metal-related corruption [5]. That is why most of these methods include pre-processing algorithms for correction of beam-hardening and other possible artifact sources [61].

Iterative reconstruction methods: These methods are mostly used to reconstruct missing parts from incomplete projections. Missing data are obtained by iterative algorithms such as Maximum Likelihood Estimation Maximization (MLEM) or Algebraic Reconstruction Technique (ART). These methods are useful in flexible modeling of the sinogram and decreasing the projection uncertainty, but they are computationally heavier than FBP [61]. Therefore, they are not preferred for commercial X-ray CT scanners in clinical use.

Reconstruction correction methods: Reconstruction correction methods are based on correction the metal artifacts on the corrupted projection data, which increases the efficiency of the method since they are carried out on reconstructed images without the need for FP and BP. Unfortunately they are only useful for correcting mild artifacts [61].

There are several issues about MAR methods that need to be considered. Firstly, MAR algorithms mostly assume the existence of a few sources of artifacts, which might not be enough to correct the image as a whole, and it might even cause additional errors on the image by altering the correct values. Furthermore, every MAR method cannot be applied for all imaging modalities because each modality has different combinations and dominance of artifacts.

In the context of this thesis, a projection completion method, inpainting, was selected for MAR due to its wide use in clinical practice. Also an iterative reconstruction method, DCT domain gap-filling method, was utilized in CT images in order to compare the performances of two different MAR techniques.

7.1. Sinogram Inpainting

As explained by Bertalmio *et al.*, the term “Inpainting” was initially used in modifying pieces of art, which was later adapted into image processing as an algorithm to change the image in an undetectable way [62]. Inpainting is based on

detecting the regions that needs to be restored and then filling these regions by using the surrounding information. It is especially useful in removing elements from an image, which in this case, high density materials such as metal fillings, crowns or braces. It is one of the most commonly used projection completion method due to its high computational efficiency. Computational flow of the inpainting algorithm in sinogram domain is demonstrated in Figure 7.1.

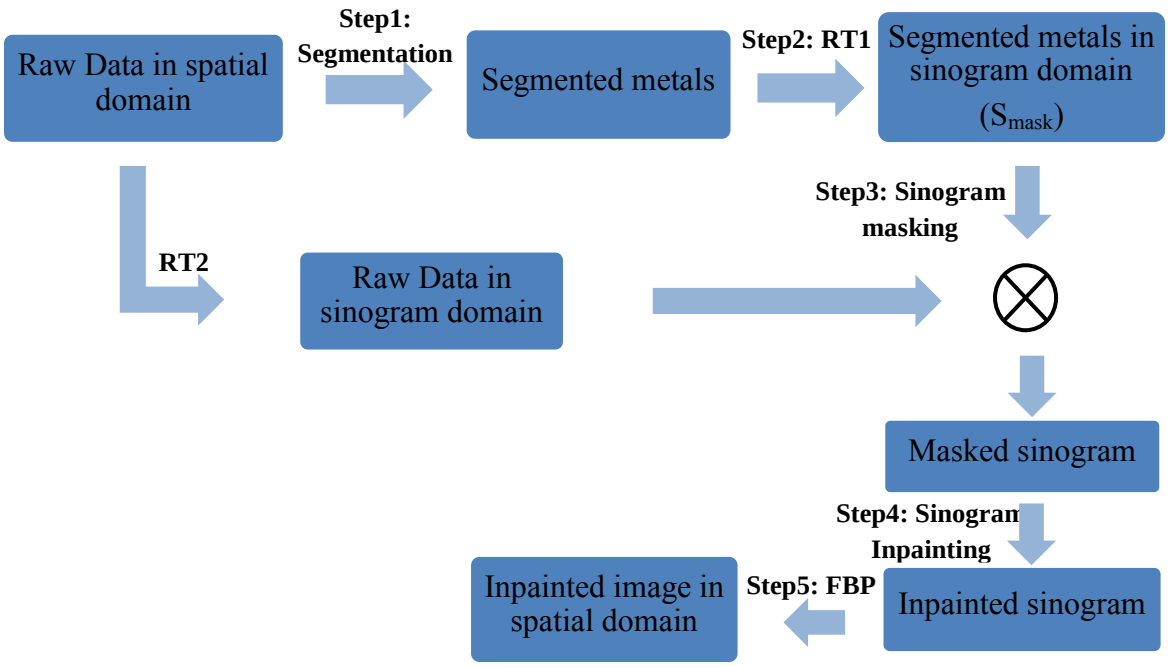

Figure 7.1: Computational flow of the MAR based on Sinogram Inpainting

Similar to most of the gap filling methods, inpainting includes three main steps: (1) generation of the sinogram mask for metal-only regions (Steps 2 in Figure 7.1), (2) masking the original sinogram with the metal-only mask (Step 3 in Figure 7.1), (3) filling the metal only parts by using the information of neighboring pixels in the original sinogram (Step 4 in Figure 7.1) [63].

7.2. Discrete Cosine Transform Domain Gap-filling Method

DCT domain gap-filling method was initially developed by Tuna *et al.* in order to compensate for the missing data parts, caused by high density objects. Idea behind this algorithm is to filter the corrupted data, which consists of high intensity values, by using a filter in DCT domain and iteratively estimating the values of the gaps. Detailed diagram of this method is presented in Figure 7.2.

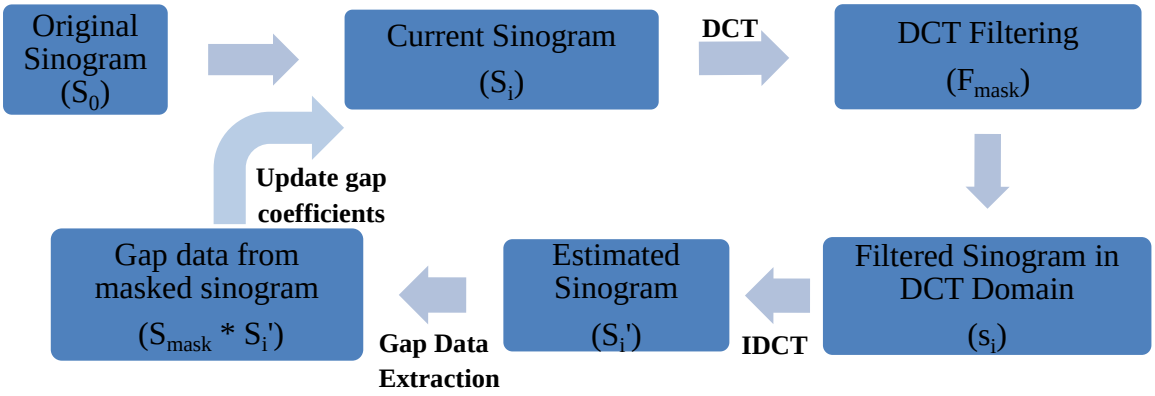

Figure 7.2: Block Diagram for DCT domain gap-filling method [Modified from [64]].

As it can be seen from Figure 7.2, the first step is to obtain the sinogram with metal artifacts, which is considered as the initial sinogram (S_i). S_i is transferred into DCT domain, where the image pixels are mapped onto DCT domain according to their frequencies. Low frequency values indicate a low rate of change between neighboring pixels, whereas high frequencies indicate sharp edges between adjacent pixels. Since metals cause instant changes in the intensity values, a DCT filter is constructed so that coefficients in this filter provide only the non-metallic intensities. The DCT mask (F_{mask}) is constructed by using these coefficients, which is explained in Tuna's work in details [65]. F_{mask} is later multiplied with the current sinogram (S_i) in DCT domain. This multiplication results in s_i, which is the image containing the non-metallic regions in DCT domain. s_i is transferred back to sinogram domain by 2D inverse DCT (IDCT), after which the estimated sinogram (S_i') is achieved. When S_i' is multiplied with the sinogram mask (S_{mask}), which was obtained from segmentation, the data lying inside the gap region is extracted. Then, these values in the gap region are added to the current sinogram, which is used as the estimation for the next iteration (S_{i+1}). Masked intensities are updated with the new values obtained from the gap data until the mean squared error (MSE) becomes smaller than a pre-determined error value. [64]

7.3. Metal Artifact Reduction on Simulated Dataset

Once the metals are segmented correctly, next step is to apply the gap filling algorithms on the sinograms. However, the slices, which do not have metal inside, should be excluded from the MAR algorithm. In order to test the existence of metals in each axial slice, a global thresholding in spatial domain was utilized. The pre-defined threshold was selected as 1.8, which was chosen to be larger than the maximum density of the anatomical structures and smaller than the previously identified metal value (Table 5.1). The slices, which contained higher values than the threshold, were subjected to MAR, otherwise they were directly reconstructed with FBP.

In order to carry out the gap filling algorithm, segmented metals sinogram depicted in Figure 6.1 was inverted and used as a mask to replace the erroneous values of metals in the original sinogram. Figure 7.3 shows the masked sinogram as

well as the resulting sinograms after two gap filling methods (DCT domain gap-filling method and Inpainting).

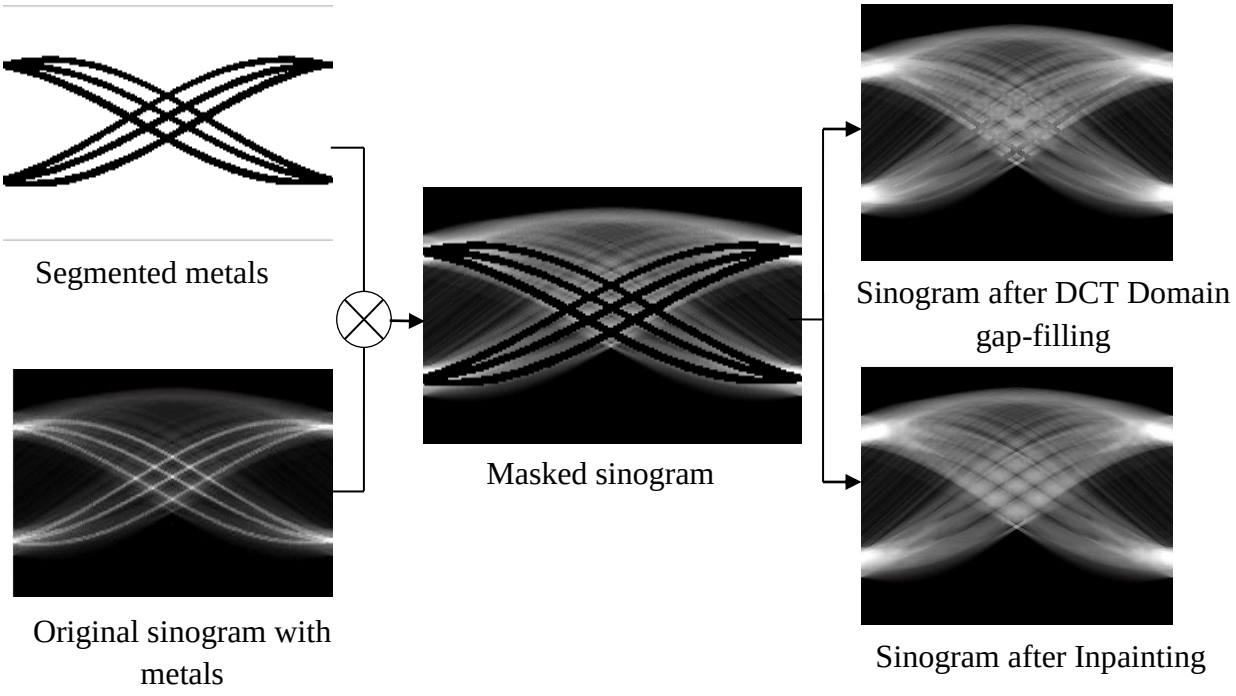

Figure 7.3: Block diagram for MAR with DCT domain gap-filling method and inpainting for β=18°. The sinogram with segmented metals is multiplied with the original sinogram in order to mask out the metal object traces. Afterwards, the masked sinogram is used as a basis for the gap filling methods.

Corrected sinograms in Figure 7.3 were later reconstructed with FBP, in which Hann window was chosen for filtering and bicubic interpolation was used for calculation of new pixel values.

7.4. Metal Artifact Reduction on Experimental Dataset

In order to apply the MAR methods on the experimental dataset, segmented sinograms in Chapter 6.4 were used to mask out the metals in S_1. Then, these masked values were reconstructed with (1) Inpainting and (2) DCT domain gap-filling methods. Three different sinogram masks, previously defined in Chapter 6, were used to mask out the metal values on the original sinogram, and both MAR methods were applied on each masked sinogram. Resulting sinograms of after MAR methods are demonstrated in Figure 7.4.

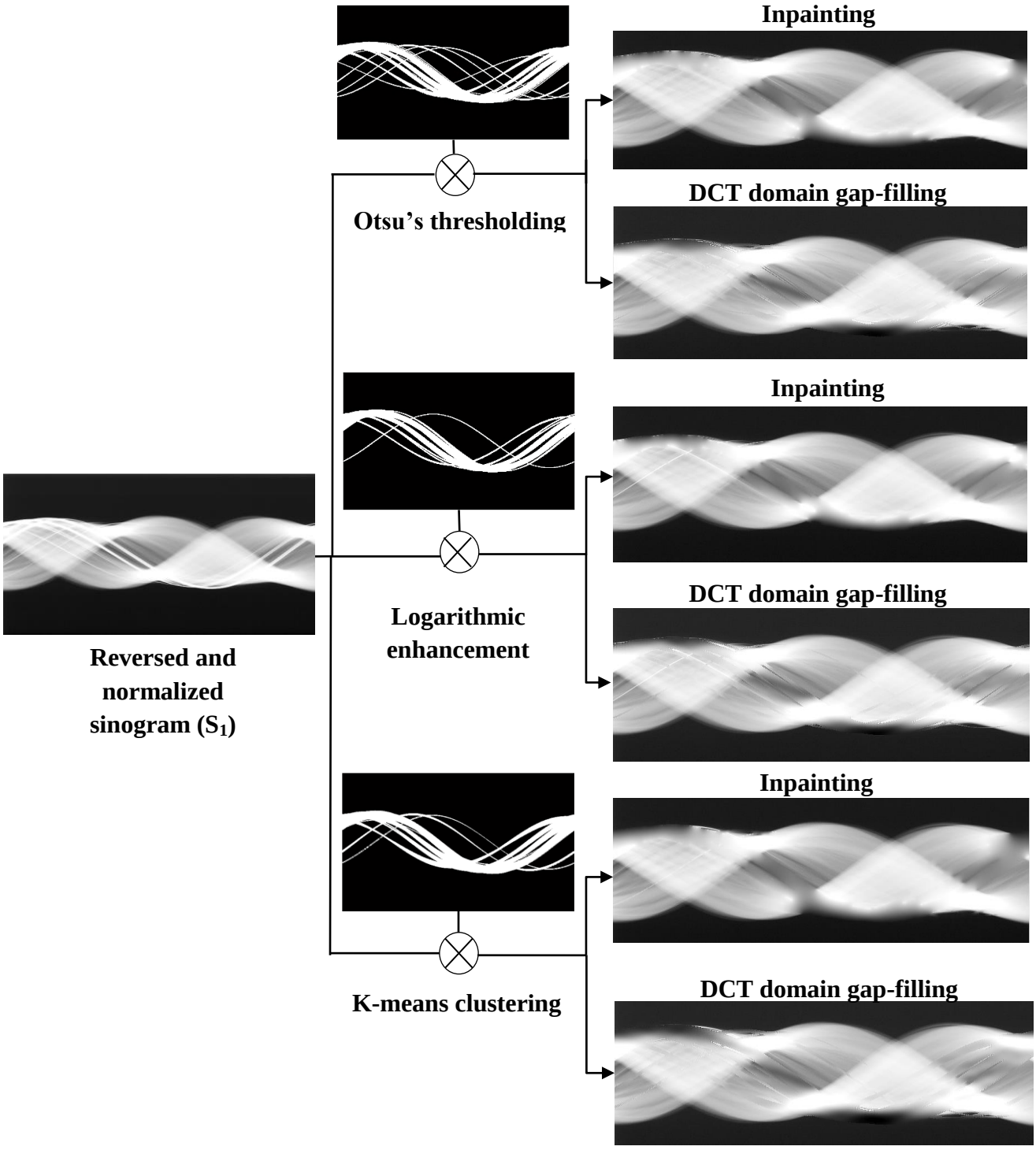

Figure 7.4: Resulting sinograms for MAR methods after different segmentation methods (Otsu's thresholding, Logarithmic enhancement, K-means clustering). Correctly segmented metal values are replaced with more realistic values, closer to the surrounding structures.

Once the sinograms were obtained after MAR, they were backprojected to spatial domain, where the performances of the segmentation and MAR algorithms were evaluated. Performances of the gap filling algorithms are compared in Chapter 9.

8. RESULTS

8.1. Results for Simulated Dataset

On the simulated dataset, both qualitative and quantitative analyses were carried out in order to assess the effect of jaw tilting, as well as the performance of MAR methods. Sample axial views of reconstructed images, which were obtained after MAR and back-tilt operations, are shown in Figure 8.1.

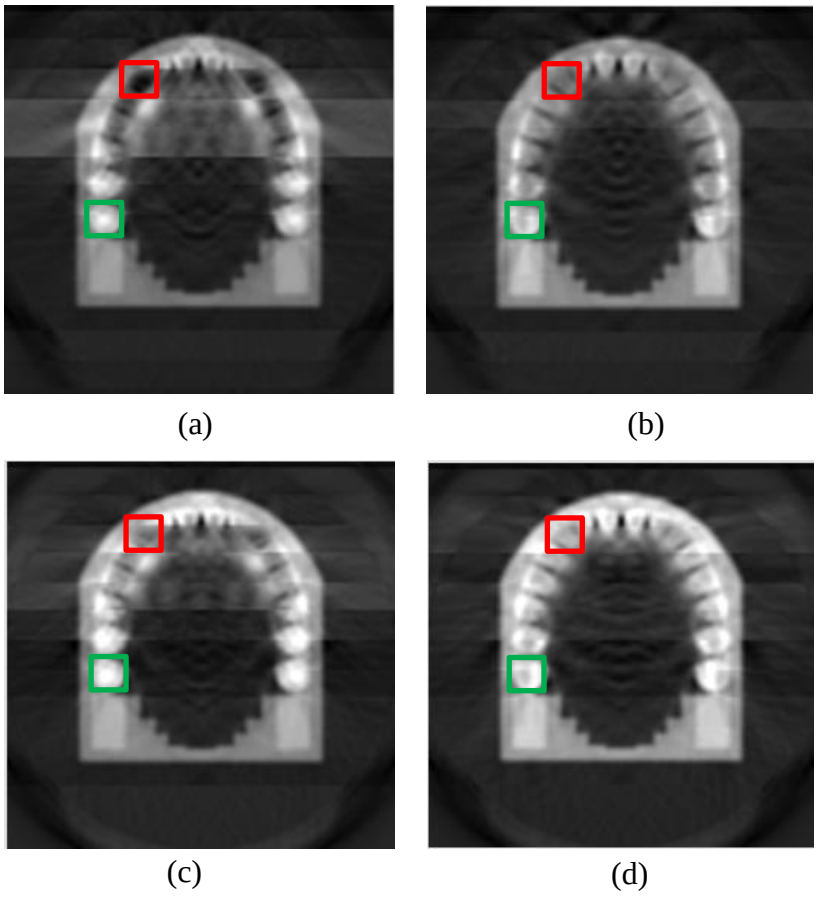

Figure 8.1: Reconstructed images for after DCT domain gap-filling for tilting with (a) α and (c) β, after inpainting for tilting with (b) α and (d) β. Areas marked with green demonstrate successful recovery of intensities for tooth as well as compensation of metal values. Areas marked with red indicate lower degree of recovery and compensation.

Slice comparison

Recovery of the intensity values around metals is considered as an important parameter for performances of MAR methods. Therefore, mean intensity values of teeth regions in certain ROIs were calculated and compared with the ground truth values in the corresponding regions. These ROIs are marked with green and red rectangles on the reconstructed images in Figure 8.1.

For jaw tilting at α=12°, mean values in green encircled regions were calculated as 0.699 and 0.724 for DCT domain gap-filling and inpainting methods respectively. Compared to the mean ground truth values calculated in the encircled regions (0.845), intensity of teeth region was slightly decreased, whereas the intensity of the metallic region was significantly lowered. Mean intensity values in the red encircled region were calculated as 0.176 and 0.420 for DCT domain gap-filling and inpainting methods respectively, which demonstrated a considerable decrease in the reconstructed values of teeth in this region.

For tilting at β=12°, mean values in the green encircled areas were calculated as 0.694 after DCT domain gap-filling and 0.721 after inpainting. These mean values indicate a significant decrease in average intensity of the metallic region and a slight decrease in the teeth region, leading to similar results with α=12°. However, in the red encircled areas mean values for DCT domain gap-filling and inpainting methods were calculated as 0.457 and 0.595, which were higher than the results obtained with α=12°, especially for DCT domain gap-filling.

Line Profile Analysis

In order to analyze the reconstruction accuracy of the values around the metallic regions, line profile analysis was carried out. Profile analysis for α variation after DCT domain gap-filling and inpainting methods are depicted in Figure 8.2 and Figure 8.3. Taking the green line, drawn on Figure 8.2 and Figure 8.3, under consideration, it can be said that intensity values of the reconstructed images became closer to the line profile of the ground truth image as α increased from 0° to 30°. Although both MAR methods clearly demonstrated an increase in reconstructed values with increased angle, further qualitative and quantitative analysis is required in order to make a more accurate observation.

Figure 8.4 and Figure 8.5 show the profile analysis for DCT domain gap-filling and inpainting methods for different β. Similar to the case of tilting with α, intensity values of the reconstructed images became closer to the ground truth profile as β was increased from 0° to 30°. Although both MAR methods provided a slight increase in reconstructed intensity values with increased β, no significant change was observed in contrast to the tilt by α.

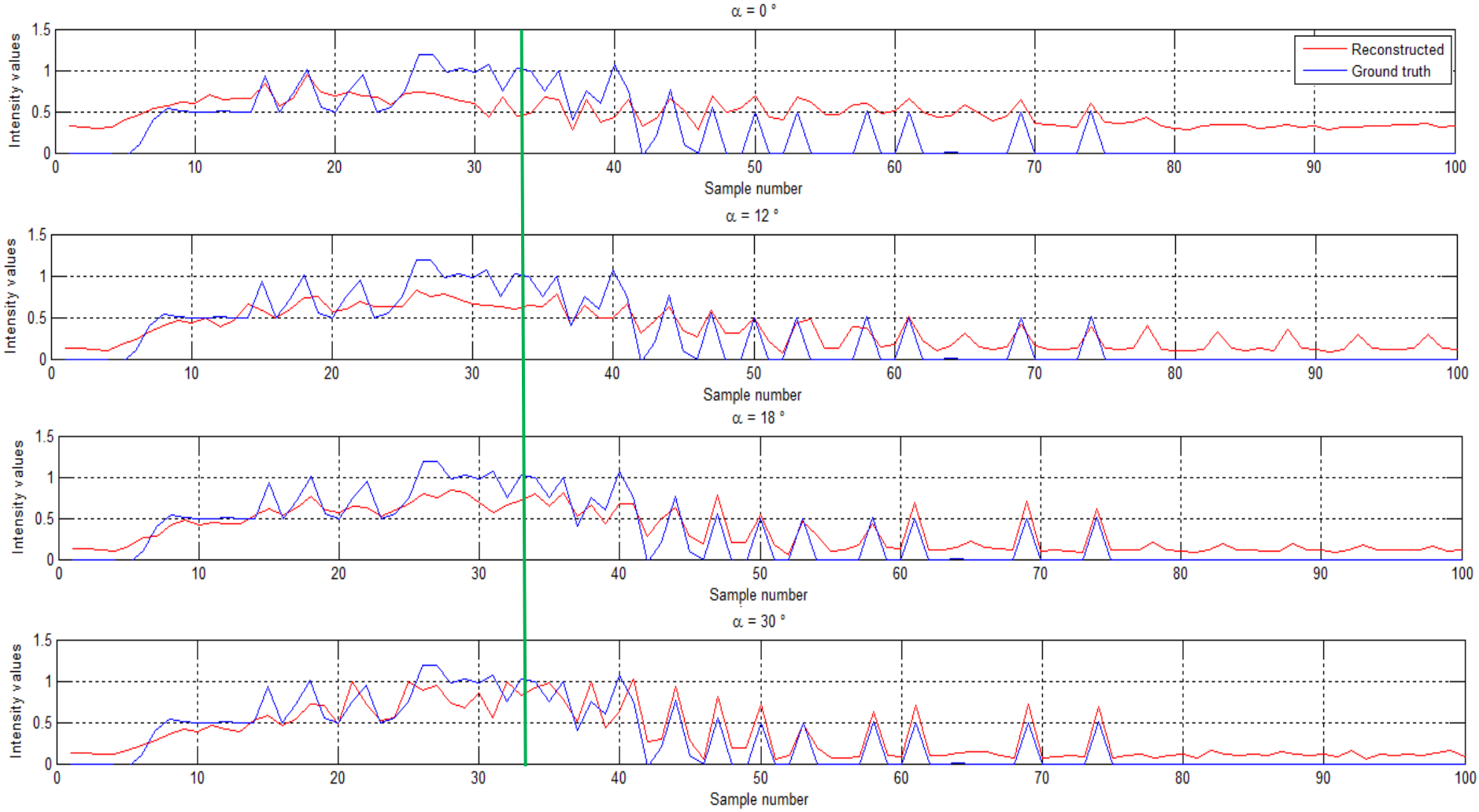

Figure 8.2: Intensity profile analysis for analysis for different α values, (blue) for reconstructed datasets and (red) ground truth image after DCT domain gap filling method.

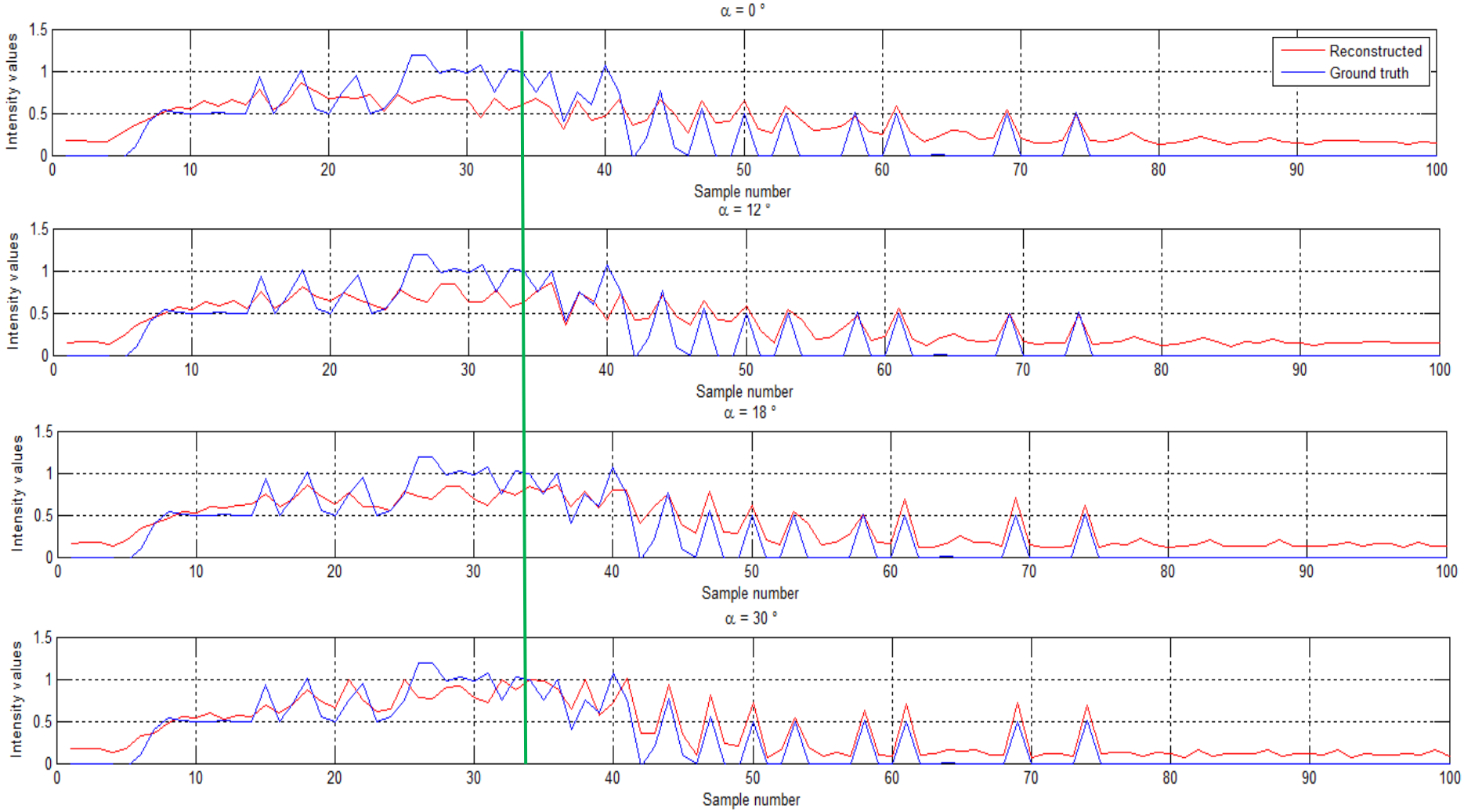

Figure 8.3: Intensity profile analysis for different α values, (blue) for reconstructed datasets and (red) ground truth image after inpainting.

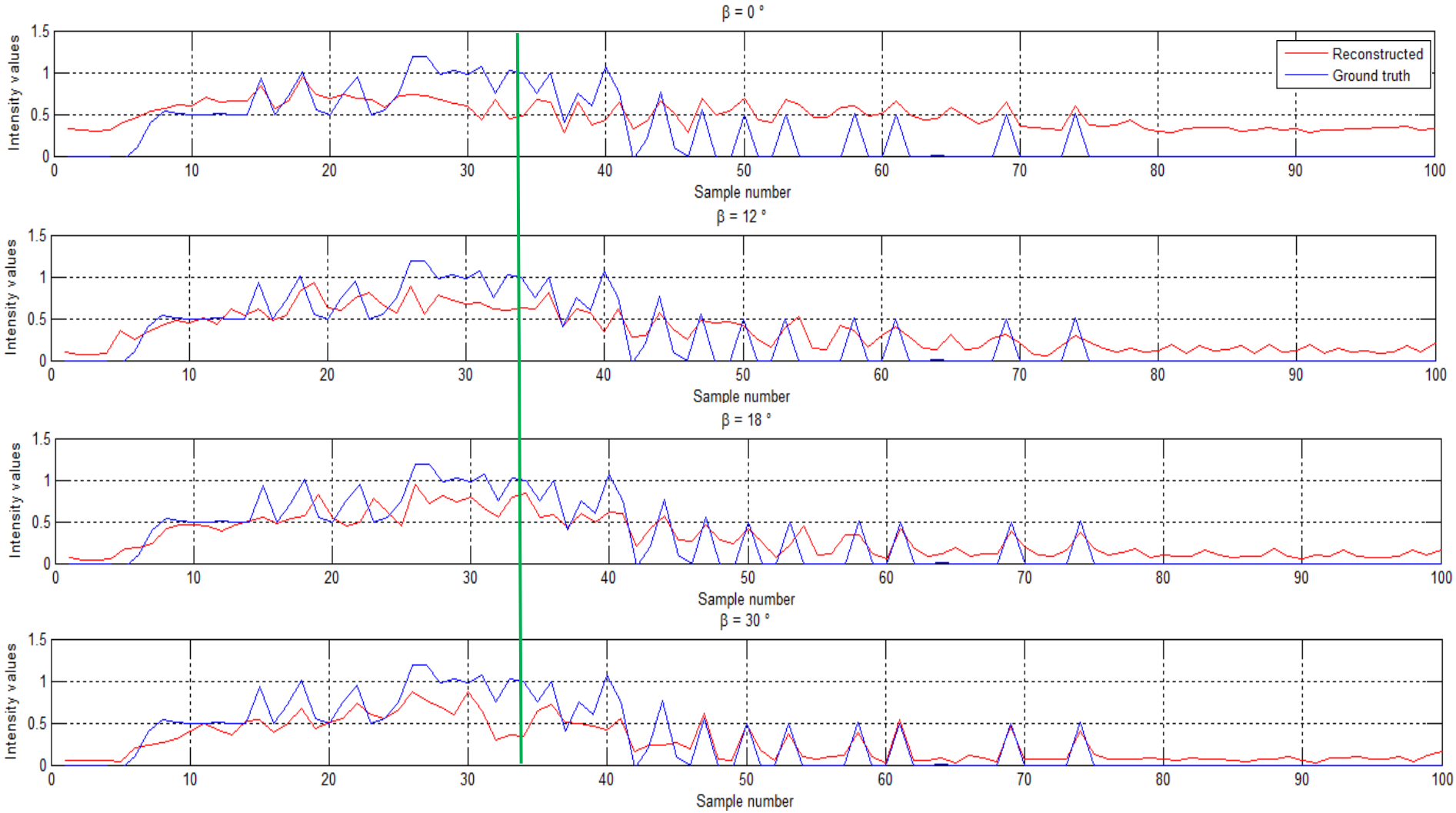

Figure 8.4: Intensity profile analysis for different β values, (blue) for reconstructed datasets and (red) ground truth image after DCT domain gap filling.

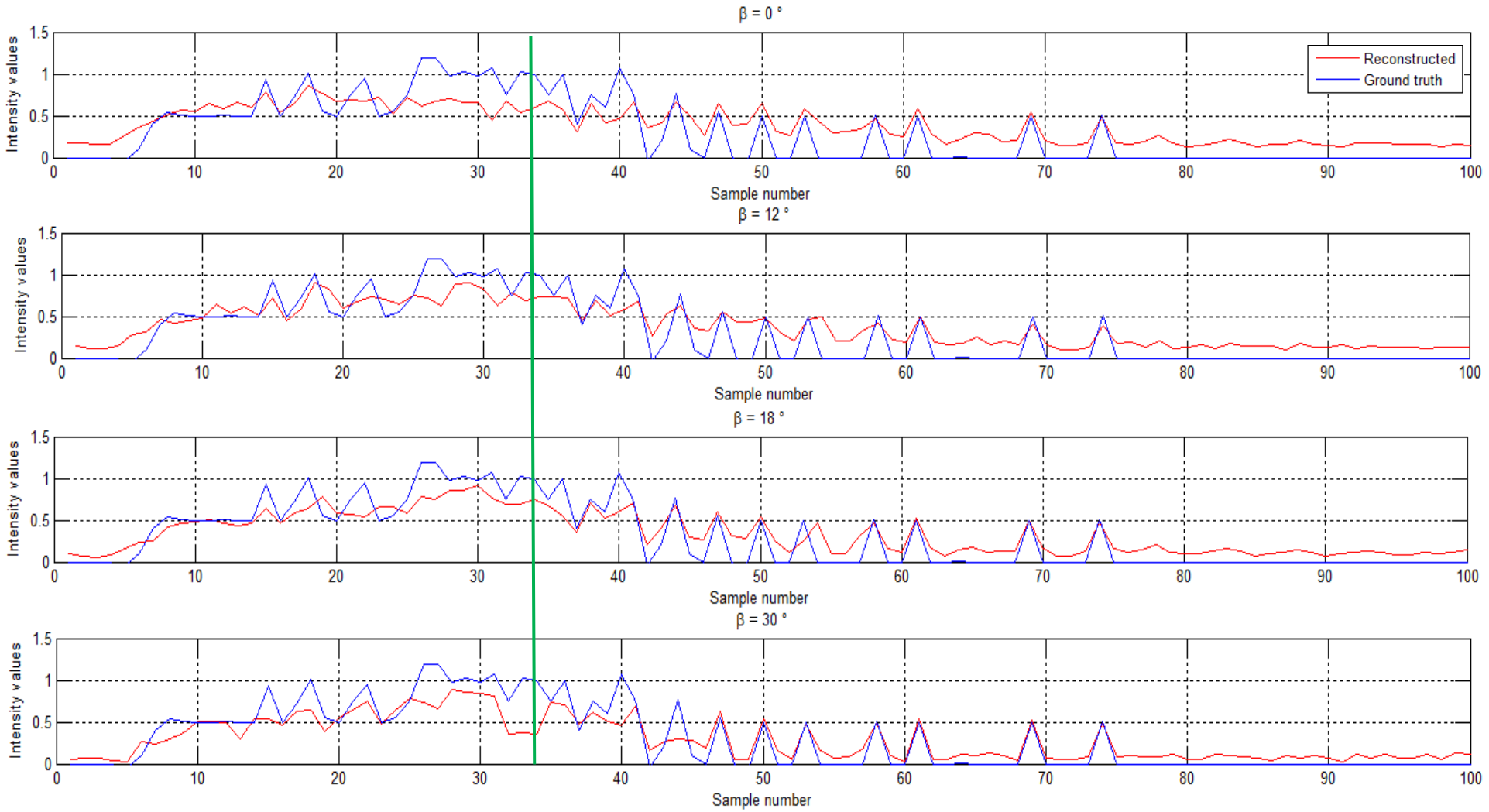

Figure 8.5: Intensity profile analysis for different β values, (blue) for reconstructed datasets and (red) ground truth image after inpainting.

Other image quality measurements

In addition to line profile analysis, other image quality measurement parameters such as PSNR, NMSE and SSIM index were calculated in order to make more accurate deductions from the quantitative analyses. Aforementioned quality measures were calculated for calculated for both α tilt (jaw opening/closing) and β (nodding) and they are presented in Table 8.1 and Table 8.2.

Tilting with α

Table 8.1 provides the values of NMSE, PSNR and SSIM index that were calculated for background, jaw and teeth regions, for 6 different values of α.

Table 8.1: Image quality assessment measures for different α values for reconstructed images, with respect to the ground truth image. The best values for each image quality measure for each region are written in bold in the table.

α	Jaw Regions	Inpainting			DCT domain gap-filling		
		PSNR (dB)	NMSE	SSIM index	PSNR (dB)	NMSE	SSIM index
0°	Background	16.419	0.0228	0.9968	10.406	0.0911	0.9871
	Jaw	28.608	0.0014	0.9999	25.574	0.0028	0.9997
	Teeth	19.933	0.0102	0.9989	18.372	0.0145	0.9984
6°	Background	16.405	0.0229	0.9968	12.328	0.0585	0.9916
	Jaw	29.361	0.0012	0.9999	25.983	0.0025	0.9997
	Teeth	19.981	0.0100	0.9989	18.298	0.0148	0.9984
12°	Background	16.550	0.0221	0.9969	15.332	0.0293	0.9958
	Jaw	**29.996**	**0.0010**	**0.9999**	**27.175**	**0.0019**	**0.9998**
	Teeth	20.795	0.0083	0.9991	18.986	0.0126	0.9987
18°	Background	17.310	0.0186	0.9974	18.224	0.0151	0.9979
	Jaw	25.834	0.0026	0.9997	25.951	0.0025	0.9997
	Teeth	21.935	0.0064	0.9993	20.214	0.0095	0.9990
24°	Background	**18.457**	**0.0143**	**0.9981**	19.645	0.0109	0.9986
	Jaw	24.069	0.0039	0.9996	23.834	0.0041	0.9996
	Teeth	20.518	0.0089	0.9991	20.120	0.0097	0.9990
30°	Background	18.363	0.0146	0.9981	**19.719**	**0.0107**	**0.9986**
	Jaw	24.281	0.0037	0.9996	24.557	0.0035	0.9996
	Teeth	**22.866**	**0.0052**	**0.9995**	**21.261**	**0.0075**	**0.9993**

When recovery levels of background intensities were evaluated for increasing angles of α, increased PSNR values were computed for both inpainting and DCT domain gap-filling methods. Also NMSE was decreased significantly, which indicates an overall improvement in noise reduction along with the increased SSIM indices for both MAR methods.

PSNR values of the jaw region initially showed a slight increase until 18°, but later it decreased to a value lower than its initial value for both inpainting and DCT domain gap-filling methods. NMSE values also showed a similar pattern by indicating a decrease in the error followed by a significant increase for both MAR methods. No significant change was observed in SSIM index for both MAR methods. This increase in error was caused by the back-tilting operation and it is discussed further in Chapter 9.

Finally, an overall increase from 0 º to 30º was observed for the PSNR values of the teeth region, with the exceptional decrease at 24º tilting in contrast with the overall pattern.

Tilting with β

Table 8.2 provides the values of NMSE, PSNR and SSIM index that were calculated for background, jaw and teeth regions, for 6 different angles of β.

Table 8.2: Image quality assessment measures for different β values for reconstructed images, with respect to the ground truth image. The best values for each image quality measure for each region are written in bold in the table.

β	Jaw Regions	Inpainting			DCT domain gap-filling		
		PSNR (dB)	NMSE	SSIM index	PSNR (dB)	NMSE	SSIM index
0°	Background	16.419	0.0228	0.9968	10.406	0.0911	0.9871
	Jaw	28.608	0.0014	0.9999	25.573	0.0028	0.9997
	Teeth	19.933	0.0102	0.9989	18.372	0.0145	0.9984
6°	Background	16.659	0.0216	0.9970	13.092	0.0491	0.9927
	Jaw	27.146	0.0019	0.9998	26.477	0.0023	0.9998
	Teeth	20.696	0.0085	0.9991	18.724	0.0134	0.9986
12°	Background	16.872	0.0205	0.9972	16.962	0.0201	0.9972
	Jaw	25.441	0.0029	0.9997	25.853	0.0026	0.9997
	Teeth	22.863	0.0052	0.9995	20.797	0.0083	0.9991
18°	Background	17.406	0.0182	0.9976	17.922	0.0161	0.9979
	Jaw	27.054	0.0020	0.9998	**26.393**	**0.0023**	**0.9998**
	Teeth	**23.634**	**0.0043**	**0.9996**	**21.996**	**0.0063**	**0.9994**
24°	Background	17.748	0.0168	0.9978	18.268	0.0149	0.9980
	Jaw	**27.823**	**0.0017**	**0.9999**	25.811	0.0026	0.9998
	Teeth	22.701	0.0054	0.9995	21.878	0.0065	0.9994
30°	Background	**18.317**	**0.0147**	**0.9981**	**19.103**	**0.0123**	**0.9984**
	Jaw	24.981	0.0032	0.9997	24.283	0.0037	0.9996
	Teeth	22.376	0.0058	0.9995	21.728	0.0067	0.9994

Based on the increasing PSNR values of the background given in Table 8.2, it can be said that a slight reduction in noise was achieved by inpainting. Although both MAR methods showed an increase in PSNR, change in PSNR values obtained from the DCT domain gap-filling was more significant compared to the inpainting. NMSE values were lowered considerably as β increased for both MAR methods. SSIM indices also supported the enhanced correlation between the ground truth and reconstructed images after both DCT domain gap-filling and inpainting methods.

When the image quality measures were calculated for the jaw region, reconstruction quality decreased with increased β. Decreased PSNR and increased NMSE values were observed for both MAR methods. Change in SSIM index was relatively small and did not follow a certain pattern; therefore SSIM index results were inconclusive for this region.

PSNR values increased in the teeth region as β increased, indicating a better reconstruction together with the decreased NMSE values for both MAR methods. Improvement in reconstruction was supported by the increased SSIM indices.

Figure 8.6 shows the reconstructed images after MAR for tilted slices. In order to visualize the performances of DCT domain gap-filling and inpainting methods, slices depicted in the figure were taken before the back-tilt.

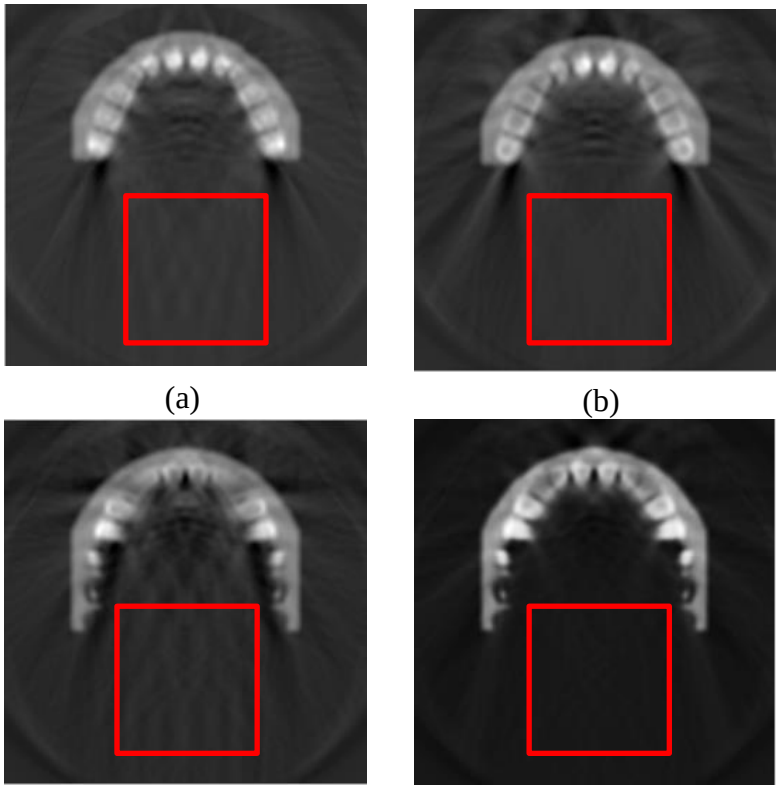

Figure 8.6: Backprojected images after DCT domain gap-filling for jaw tilting with (a) α and (c) β, after Inpainting for jaw tilting with (b) α and (d) β (α=β=18°). In the red encircled areas, DCT domain gap-filling induce new artifacts for both α and β, whereas none of those artifacts were observed after inpainting.

After DCT domain gap-filling method, metal values were closer to the intensity of teeth compared to the reconstructed values from inpainting for jaw tilting with both α and β (Figure 8.6). However, additional artifacts were observed in the encircled areas in for DCT domain gap-filling method (Figure 8.6.a and Figure 8.6.c), which was non-existent after inpainting (Figure 8.6.b and Figure 8.6.d).

When reconstruction of 3D slices is considered, it is important to remember that only the slices that contained metal fillings were subjected to MAR, whereas slices with no metal were directly backprojected into spatial domain, which was mentioned in Chapter 6.3. This separation naturally caused a difference between reconstructed slices with and without MAR, and this difference is demonstrated in Figure 8.7.

Values of reconstructed teeth and jaw regions varied slightly between Figure 8.7.a and Figure 8.7.b, but a significant change was observed for the background intensities. Although this phenomenon was observed in both tilting cases, only reconstructed slices from tilting with α is presented in Figure 8.7 as an example of change in the background intensities.

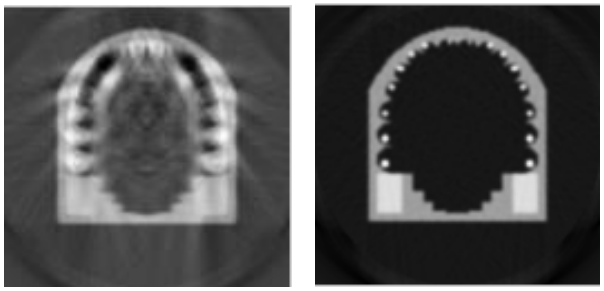

(a) (b)

Figure 8.7: Examples of (a) reconstructed and back-tilted slice with metals (DCT domain gap-filling) and (b) reconstructed slice with no metals. Contrast difference between the backgrounds of two images can be clearly seen.

Back-tilting operation, which was applied on the reconstructed 3D phantom after MAR, created some dark horizontal lines, which are shown in Figure 8.8.

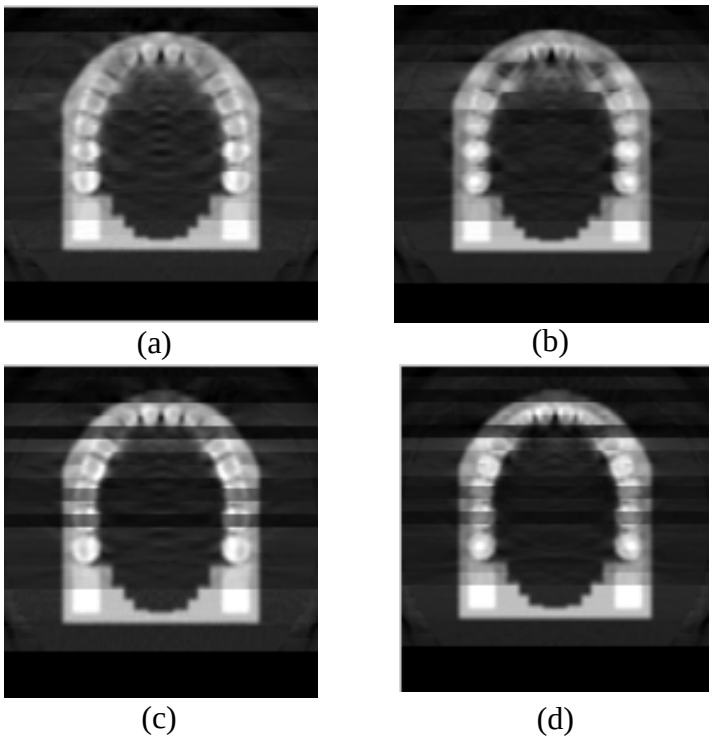

(a) (b)

(c) (d)

Figure 8.8: Back-tilted images for (a, b) α=18°, (c, d) α=24° after (a, c) inpainting and (b, d) DCT domain gap-filling methods

These lines become prominent at tilts greater than 18°, and possible reasons for these dark lines are discussed further in Chapter 9.

8.2. Results for Experimental Dataset

In this section, results obtained from different segmentation and MAR methods are presented. Firstly, segmentation methods are compared qualitatively based on the resulting segmented sinograms. Afterwards, quantitative evaluation of overall MAR algorithms was carried out based on the means and standard deviations of different ROIs.

According to the segmented sinograms and their respective backprojected images, which were obtained in Chapter 6.4, it was observed that Otsu's thresholding method was successful in segmenting the metallic parts, but parts of jaw bones were falsely detected along with the metals after the thresholding in the spatial domain. Also segmented metallic regions on the sinogram were observed to be slightly larger than the actual metal traces. With logarithmic enhancement, all metals except one were detected. Moreover, there were no falsely detected structures. The areas of segmented regions were also closer to the real imprints of metals on the original sinogram than other segmentation methods. For k-means clustering, all the metals were segmented without any additional structures. However, due to the dilation, which was used to correct the missing points on the segmented sinogram, thickness of the metallic traces increased.

MAR methods

Table 8.3, presents the mean values and standard deviations after inpainting and DCT domain gap-filling methods, that were applied posterior to the segmentation methods.

Table 8.3: Mean and standard deviation values of the uncorrected image

	Regions	**Mean**	**Standard Deviation**
Uncorrected image	1	62.488	11.761
	2	64.124	36.219
	3	43.786	22.796
	4	5.776	2.842
	5	14.15	3.202

Values shown in this table do not correspond directly to HU values since they were calculated on the backprojected spatial image. However, they provide valid information for the comparison of several techniques that were utilized in this thesis. It should be noted that, in the calculation of the values given in Table 8.3, negative values caused by the FBP were not included. Region numbers, which are referred in this table, were defined earlier in Figure 5.9. Mean and standard deviation values for different regions are provided in Table 8.4, which are later compared with the values obtained from the reconstructed images.

Table 8.4: Mean and standard deviation values for segmentation and MAR methods. The best mean and standard deviation results for each region are written in bold.

		Inpainting		DCT domain gap-filling	
	Regions	**Mean**	**Standard Deviation**	**Mean**	**Standard Deviation**
Otsu's thresholding	1	54.389	**10.751**	69.354	12.321
	2	36.756	**9.556**	40.208	18.929
	3	45.134	11.246	47.841	13.573
	4	**5.652**	2.837	4.896	2.948
	5	14.192	3.479	13.118	3.755
Logarithmic Enhancement	1	**62.759**	11.512	68.592	**11.074**
	2	**45.752**	12.154	**44.029**	19.885
	3	**45.797**	13.764	**51.019**	16.133
	4	5.535	**2.770**	**5.154**	**2.744**
	5	13.423	3.488	12.745	3.831
K-means clustering	1	50.921	11.056	**69.662**	15.060
	2	29.395	10.866	36.019	**18.245**
	3	43.346	**9.297**	42.523	15.245
	4	5.549	2.875	4.746	2.872
	5	**14.640**	**3.611**	**13.769**	**3.707**

Region 1 was used to investigate the effect of MAR methods on the teeth region. According to Table 8.4, the closest mean and standard deviation values to the uncorrected image for region 1 were calculated with the combination of logarithmic enhancement and inpainting methods.

Region 2 consisted of 3 metals, which were the largest pieces of the braces on the image; therefore high mean and standard deviation were observed in this region. Since all the metals in this region were segmented successfully by all three segmentation methods, resulting mean and standard deviation values were rather close to each other. However, it was observed that inpainting provided a lower standard deviation compared to DCT domain gap-filling. The expected mean value for region 2 after reconstruction would be close to the mean value of region 1 after MAR, since they both essentially include the teeth region, but with low standard deviation. The most accurate reconstruction with considerably low standard deviation was observed after logarithmic enhancement and inpainting, where the mean value was the highest and the standard deviation was almost one third of the uncorrected image.

Region 3 was affected by metal artifacts from several metals on the uncorrected image, which caused a high standard deviation in the region. After MAR, mean values remained unchanged, which was expected since the region did not include any metals in it. However, the standard deviation after MAR was decreased by almost %50, indicating a considerable decrease in the streaking affects. The combination of Otsu's thresholding and DCT domain gap-filling provided the highest mean, but not the lowest standard deviation. On the other hand, Otsu's thresholding with inpainting resulted in the lowest standard deviation with relatively high mean.

Region 4 was chosen near two metal pieces, and was assumed to be subjected to streak artifacts. However, since the metals were small, together with the low dosage of CBCT exposure, they did not cause major artifacts. Due to the insignificance of the

artifacts, none of the segmentation and MAR methods significantly lowered the standard deviation.

Region 5 was used to investigate the effect of MAR methods on the reconstruction of the inner jaw. As it can be observed from stable constant mean and standard deviation values, no additional artifacts were introduced by either MAR methods.

9. DISCUSSION AND CONCLUSION

9.1. Simulated Dataset

Jaw Tilting

The aim of tilting the jaw in the source-detector place was to prevent coplanarity by reducing the overlap of metals on each slice. Although both tilting methods enhanced the MAR, line profile analysis among the two proposed tilting methods showed that tilting by α was more effective in the reconstruction compared to tilting by β. This conclusion was also supported by the study of Lucklow *et al.*, which found the tilting by α more beneficial for decreasing metal artifacts in CBCT images [6].

Improved performance of MAR with the jaw tilt can be explained with the decrease of surface areas of metals in each tilted slice. As it can be seen in Figure 9.1, all 16 metals are visible on the non-tilted image in Figure 9.1.a, whereas 6° tilted image in Figure 9.1.b shows only 8 metals instead of 16.

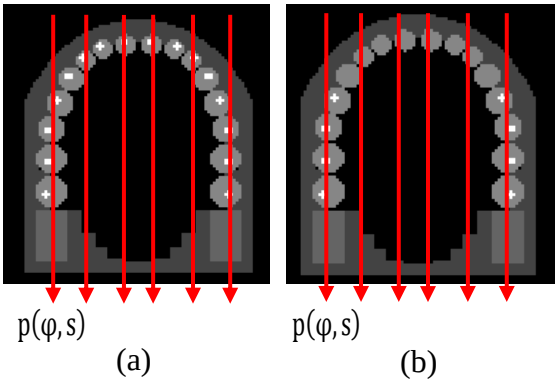

Figure 9.1: (a) Non-tilted, (b) tilted with α= 6° axial views of the jaw phantom. From the comparison of (a) and (b), it can be seen that projection vectors p(φ,s) pass through fewer metal fillings on the tilted image.

As the number of metals in each slice decreases, amount of metals in each projection vector *p(φ,s)* decreases, leading to fewer metal imprints on the sinogram domain. Thus, gap-filling methods result in a more accurate correction of metallic regions by using more information from the surrounding anatomical structures in the image.

Based on the line profile analysis and other quality measurements, it was concluded that reconstruction of teeth regions was enhanced by increased α. Moreover, with a higher α, a better fit to the ground truth line, was observed in the jaw regions compared to β tilt.

In order to understand the superiority of α tilt over β tilt, it is important to consider the mandible and maxilla from a coronal view rather than axial view. As it can be seen in Figure 9.2.a, center of rotation (COR) shifts when the jaw is tilted with β (COR_1). However, in the case of α tilt, center of rotation (COR_2) remains the same for all tilting angles. This shift in COR is different for every β value, which changes the number and position of the slices in each tilted 3D phantom. Therefore, line profile analysis, which

is carried out on the same slice for each reconstructed phantom, does not only represent the angle of tilt, but it also includes the effect of shift in COR. As a result, values that are obtained from this analysis for β cannot be used as a direct measure of enhancement in MAR via tilting. If the COR can be fixed for different β, then the line profile analysis from the slices would provide a more accurate comparison. It should be noted that this shift in COR only occurred because of the rotation function used in this thesis, which can be corrected with further work on the rotation algorithm. For the real life images, COR would remain the same for all tilts.

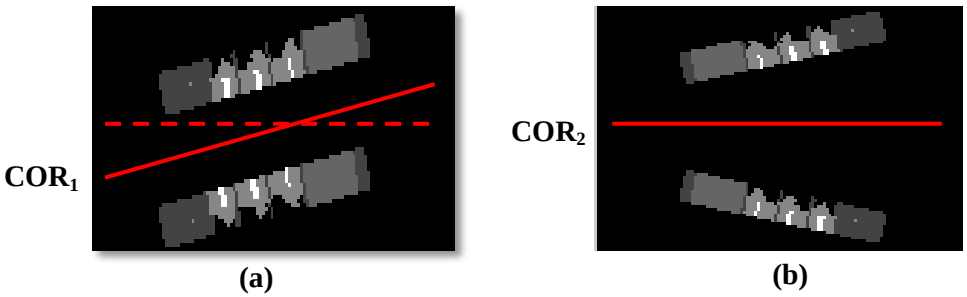

Figure 9.2: Sample COR lines for the jaw tilted with (a) β and (b) α on the coronal view of jaw phantom. In (a), the original COR is shown with dashed line, whereas COR_1 represents the COR after β tilt. COR remains the same after α tilt.

According to the results of quantitative assessment on the simulated dataset, an α between 24° and 30° is recommended. Between 24° and 30°, the error values for the reconstructed teeth and background regions were calculated to be the smallest. This tilting range was also supported by the findings of Lucklow *et al.*, who determined the ideal tilting angle for the mandible as 14°, corresponding to an α of 28°. Lucklow *et al.* also mention that rearrangement of the teeth with an angle of 14º can reduce the exposure time and related dose to one forth. Although a decrease was observed in the reconstruction quality of the jaw region, utilization of a different interpolation technique in tilting can increase the quality of the reconstruction in this region as well.

MAR methods

When slices were tilted back after MAR, slices with different backgrounds were interpolated together, which caused relatively dark and bright lines on the back-tilted image, demonstrated in Figure 8.8. Although tilting improved the MAR results, these dark horizontal lines observed after back-tilting for high degree tilts (α > 18º) decrease the overall image quality. Most of these dark lines are caused by different offsets of background intensities on different slices. Although a small deviation from the average reconstructed values was expected between slices depending on whether MAR was applied or not, darkest lines observed in Figure 8.8.b and Figure 8.8.d are more likely to be caused by segmentation errors on a few slices. In order to decrease the effect of these lines, use of another interpolation method (bicubic or bilinear) can be beneficial. Since these methods calculate the interpolation over a larger neighborhood, sharp contrast changes would decrease with averaging.

When reconstructed values for the regions given in Figure 8.1 are compared, it can be said that DCT domain gap-filling method had slightly higher mean values. This can be explained by the iterative nature of DCT domain gap-filling method, which helps the

more accurate estimation of reconstructed values. However DCT domain gap-filling method is computationally heavy and the difference between intensity values of two MAR methods is not large enough to choose DCT domain gap-filling method over inpainting. In addition to the computational burden, mean values obtained from Figure 8.1 indicate a greater deviation within the same structures for DCT domain gap-filling method, whereas this deviation is smaller for inpainting. This high rate of change is also supported by the NMSE and PSNR values of DCT domain gap-filling, meaning that tilting has more effect on the DCT domain gap-filling algorithm. This conclusion can be explained by the fact that fewer metals in each slice lead to fewer high frequency values to be eliminated by the DCT filter, resulting in improved reconstruction of anatomical structures. However, when there are many metals, efficiency of the algorithm decreases significantly. On the other hand, inpainting algorithm always uses the same neighborhood around the metal, which is less prone to the number of metals. As a result of these comparisons, it was concluded that inpainting was preferred over DCT gap-filling method due to its more stable and faster algorithm.

Based on the results obtained on the simulated dataset, it can be said that tilting offers a significant chance for enhancing the quality of MAR algorithms. In order to achieve better results, back tilting operation needs to be developed further with different interpolation techniques.

9.2. Experimental Dataset

The purpose of using an experimental dataset was to test different segmentation methods and MAR algorithms on a dental CT image (CBCT) and compare their performances.

Based on the qualitative comparison between simulated and experimental dataset, it was observed that performance of the MAR algorithms were not as effective as the simulated dataset when they were applied on experimental dataset, due to the properties of the provided CBCT dataset.

First of all, it is important to note that a simulated dataset includes certain, pre-determined intensity values, which makes the segmentation methods much more efficient. However, uncertain and non-standardized HU values in the experimental dataset introduce a challenge for the segmentation of different regions and structures in the image.

One of the problems encountered in the experimental dataset was the relatively low dosage of radiation (~60kV) from Promax CBCT device. Although low dosage prevented the severe artifacts, it also decreased the intensity difference between metal and bone. As it can be seen from Figure 9.3, gray level values of the metal in the encircled region are almost impossible to differentiate from bone. Therefore, it was concluded that slight increase in the radiation dosage would significantly increase the efficiency of segmentation and MAR methods on CBCT images by providing a larger intensity difference between bone and metal.

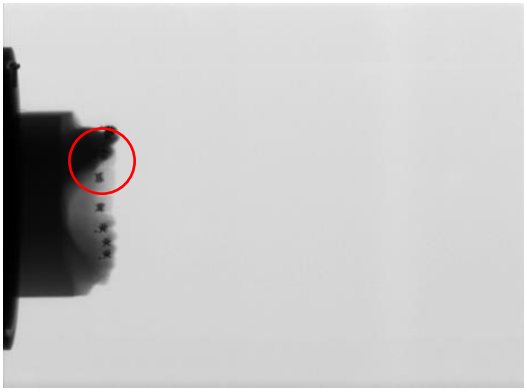

Figure 9.3: A slice from CBCT projection data of jaw. Bone and metal intensities are particularly close to each other in the marked region above.

Lack of some parameters and tools for the cone beam image reconstruction also caused additional difficulties for MAR. For instance, in clinical applications, reconstruction and artifact removal is generally conducted with the software developed specifically for the imaging product, considering all the parameters and variables of that specific device. Unfortunately in our experimental dataset, MATLAB was used for all image processing methods, which excluded some of the geometric considerations such as beam geometry, contrast enhancements and artifact reduction methods applied on the image at the time of acquisition, which were applied on the dataset beforehand.

Utilization of some simplifications in the developed image processing algorithm might have introduced additional artifacts in the image reconstruction. For instance, in a CBCT, imaging is based on cone beam technology; therefore cone beam reconstruction algorithms such as FDK are used for image reconstruction. However, in this thesis MAR methods were carried out by using FBP algorithm, which is a simplified version of FDK, and it is based on parallel beam geometry instead of cone beam. Although FBP was commonly used for CT image reconstruction because of fast image reconstruction and ease of implementation, new technology CTs, *i.e.* CBCT, with finer resolution, greater volume coverage, faster scan times and lower radiation doses push the FBP method to its limits [66]. Therefore use of FBP in this thesis gradually introduced additional artifacts in the reconstructed images.

Despite of the aforementioned issues with the dataset and the algorithm, the segmentation methods were successfully compared based on their reconstruction qualities. It was concluded that logarithmic enhancement was preferred over k-means clustering and Otsu's thresholding algorithms due to its simplicity, high mean and low standard deviation values in most of the regions. Although one of the metals could not be detected with logarithmic enhancement method, the reason for that can be explained by the discontinuity of that metal throughout the sinogram, which decreased the intensity of the region when the image was smeared back with FBP. Also, based on the mean and standard deviation values of two MAR methods, although DCT domain gap-filling resulted in slightly higher mean values, inpainting was preferred due to its lower standard deviation in almost all regions, similar to the conclusion obtained from the simulated dataset results.

In conclusion, all thresholding methods applied on the experimental dataset successfully segmented out the metals with continuous metal imprint on the sinogram. Otsu's thresholding algorithm, developed and implemented in this thesis for the experimental dataset, was employed on the constructed 3D jaw phantom for metal segmentation, and this work has been submitted to 2013 IEEE Nuclear Science Symposium and Medical Imaging Conference [67].

10. REFERENCES

[1] K. Kobayashi, A. Katsumata, I. Koichi and T. Aoki, “A Practical Method to Reducing Metal Artifact for Dental CT Scanners,” in *19th International Conference on Pattern Recognition*, Florida, 2008.

[2] A. Gahleitner, G. Watzek and H. Imhof, “Dental CT: imaging technique, anatomy, and pathologic conditions of the jaws,” *European Radiology,* vol. 13, pp. 366-376, 30 April 2002.

[3] G. Achermann, “How will dentistry look in 2020?,” Straumann, Amsterdam, 2012.

[4] R. A. Glenner and P. Willey, “Fauchard.org,” Pierre Fauchard Academy, 2 July 1998. [Online]. Available: http://www.fauchard.org/history/articles/jdh/v46n2_july98/dental_fillings_jdh_98_46_2p71.html. [Accessed 1 April 2013].

[5] B. D. Man, J. Nuyts and P. Dupont, “Reduction of metal streak artifacts in x-ray computed tomography using a transmission maximum a posteriori algorithm,” *IEEE Transactions on Nuclear Science,* vol. 47, no. 3, pp. 977-981, 2000.

[6] M. Luckow, H. Deyhle, F. Beckmann, D. Dagassan-Berndt and B. Müller, “Tilting the jaw to improve the image quality or to reduce the dose in cone-beam computed tomography,” *European Journal of Radiology*, pp. 1-5, 4 October 2010.

[7] J. Jan, “X-ray Computed Tomography,” in *Medical Image Processing, Reconstruction and Restoration*, Boca Raton, Taylor & Francis, 2006, pp. 155-175.

[8] A. G. Farman and W. C. Scarfe, “The Basics of Maxillofacial Cone Beam Computed Tomography,” *Seminars in Orthodontics*, vol. 15, no. 1, pp. 2-13, 2009.

[9] C. Celenk and P. Celenk, “Bone Density Measurement Using Computed Tomography,” in *Computed Tomography - Clinical Applications*, Rijeka, InTech, 2012, pp. 123-136.

[10] A. C. Kak and M. Slaney, “Algorithms for Reconstruction with Nondiffracting Sources,” in *Principles of Computerized Tomographic Imaging*, New York, IEEE Press, 1999.

[11] B. D. MAN, "Iterative Reconstruction for Reduction of Metal Artifacts in Computed Tomography", Ph.D. dissertation, Department Elecktrotechniek, Leuven, Belgium: Katholieke Universiteit Leuven, 2001.

[12] A. Averbuch and Y. Shkolnisky, "3D Fourier based discrete Radon transform," *Applied and Computational Harmonic Analysis,* vol. 15, pp. 33-69, 2002.

[13] U. Tuna, "Cosine domain gap-filling for the PET sinograms," M.Sc. Thesis, Department of Signal Processing, Tampere University of Technology, Tampere, 2008.

[14] S. W. Smith, The Scientist and Engineer's Guide to Digital Signal Processing, San Diego: California Technical Publishing, 2002.

[15] J. Fessler, "Analytical Tomographic Image Reconstruction Methods," in *Image Reconstruction: Algorithms and Analysis* , Michigan, The University of Michigan, 2009, pp. 1-47.

[16] T. Peters, "CT Image Reconstruction," Robarts Research Institute, Montreal, 2002.

[17] G. T. Herman, "BackProjection," in *Fundamentals of Computerized Tomography*, New York, Springer, 2009, pp. 125-133.

[18] A. J. Nygren, "Owlnet.rice.edu.tr," CDT, 8 May 1997. [Online]. Available: http://www.owlnet.rice.edu/~elec539/Projects97/cult/node3.html#SECTION0002100000000000000. [Accessed 12 March 2013].

[19] B. F. Hayden, "University of Edinburgh School of Informatics," University of Edinburgh School of Informatics, 10 February 2005. [Online]. Available: http://homepages.inf.ed.ac.uk/rbf/CVonline/LOCAL_COPIES/AV0405/HAYDEN/Slice_Reconstruction.html. [Accessed 22 April 2013].

[20] L. W. Goldman, "Principles of CT and CT Technology," *Journal of Nuclear Medicine Technology,* vol. 35, pp. 115-128, 2007.

[21] "Conference of Radiation Control Program Directors," Radiation Control Program Directors, 2011. [Online]. Available: http://www.crcpd.org/2011AnnualMeeting/Training/Sun%200800%20Strauss%20CRCPD%20Basic%20Physics%20of%20CT%205-15-11.pdf. [Accessed 2013 March 4].

[22] J. F. Barrett and N. Keat, "Artifacts in CT: Recognition and Avoidance," in *RadioGraphics*, 2004, pp. 1679-1691.

[23] V. Montemayor, "Middle Tennessee State University PHYS-400," Middle Tennessee State University, 27 January 2010. [Online]. Available:

http://capone.mtsu.edu/phys4600/Syllabus/CT/Lecture_5/lecture_5.html. [Accessed 21 March 2013].

[24] D. M. A. Alshehri, D. H. M. Alamri and D. M. A. Alshalhoob, "CBCT applications in dental practice: A Literature Review," *CAD/CAM*, 2010.

[25] J. J. Abrahams, "Dental CT Imaging: A Look at the Jaw," *Radiology 2001*, vol. 219, no. 2, pp. 334-345, 2001.

[26] M. Lahutte-Auboin, A. Ait-Ameur and V. Decat, "Dental Implant Imaging: How CT Scan Became a Help to Surgery," in *Implant Dentistry – A Rapidly Evolving Practice*, Paris, 2012, pp. 267-286.

[27] "Dental uses of CBCT," Sedentexct, [Online]. Available: http://www.sedentexct.eu/content/dental-uses-cbct. [Accessed 22 02 2013].

[28] W. C. Scarfe, M. D. Levin and D. Gane, "Useof ConeBeamComputedTomography in Endodontics," *International Journal of Dentistry*, pp. 1-20, 2009.

[29] W. D. Associates, "WoodDental.com," DukeNetNuke, 2008. [Online]. Available: http://www.wooddental.com/Technology/ConeBeamComputedTomography/tabid/155/Default.aspx. [Accessed 08 03 2013].

[30] I. Ibraheem, "Reduction of artifacts in dental cone beam CT images to improve the three dimensional image reconstruction," vol. 5, 2012.

[31] M. A. G. Silva, a. U. Wolf, F. Heinicke, A. Bumann, H. Visser and E. Hirsch, "Cone-beam computed tomography for routine orthodontic treatment planning: A radiation dode Evaluation," Goias, Leipzig, Berlin and Oldenburg, 2008.

[32] M. I. John B. Ludlow, "Comparative dosimetry of dental CBCT devices and 64-slice CT for oral and maxillofacial radiology," *Oral Surgery, Oral Medicine, Oral Pathalogy, Oral Radiology and Endodontology*, vol. 106, no. 1, pp. 106-114, 2008.

[33] J. Mah, "The Genesis and Development of CBCT for Dentistry," 2010.

[34] U. o. Manchester, "Technical Description of CBCT," Sedentexct, University of Manchester, [Online]. Available: http://www.sedentexct.eu/content/technical-description-cbct. [Accessed 22 02 2013].

[35] D. C. Hatcher, "Operational Principles for CBCT," vol. 141, no. 3, 2010.

[36] A. Freeman, "ConeBeam.com," ConeBeam.com, 8 February 2011. [Online].

Available: http://www.conebeam.com/comparison. [Accessed 05 May 2013].

[37] F. Esmaeili, M. Johari, P. Haddadi and M. Vatankhah, "Beam Hardening Artifacts: Comparison between Two Cone Beam Computed Tomography scanners," *Journal of Dental Research, Dental Clinics, Dental Prospects,* vol. 6, no. 2, pp. 49-53, 2012.

[38] P. Mah, T. Reeves and W. McDavid, "Deriving Hounsfield units using grey levels in cone beam computed tomography," *Dentomaxillofacial Radiology,* vol. 39, pp. 323-335, 2010.

[39] S. Zha, D. D. Robertson, G. Wang, B. Whiting and K. T. Bae, "X-Ray CT Metal Artifact Reduction Using Wavelets: An Application for Imaging Total Hip Prostheses," *IEEE Transactions on Medical Imaging,* vol. 19, no. 12, pp. 1238-1247, 2000.

[40] D. J. Ludlow and D. S. Brooks, "The use of cone-beam computed tomography in dentistry," The Journal of the American Dental Association, Chicago, 2012.

[41] R. Schulze, U. Heil, D. Grob and D. Bruellmann, "Artefacts in CBCT: a review," *Dentomaxillofacial Radiology,* vol. 40, pp. 265-273, 2011.

[42] M. F. McNitt-Gray, "Tradeoffs in Image Quality and Radiation Dose for CT," *Medical Physics,* vol. 33, no. 6, pp. 1-8, 2006.

[43] Q. Luo, "Artifacts in X-ray CT," Research Imaging Center, University of Texas Health Science Center, Texas, 2003.

[44] V. Naranjo, R. Lloréns, M. Alcaniz and F. López-Mir, "Metal artifact reduction in dental CT images using polar mathematical morphology," *Computer methods and programs in biomedicine,* vol. 102, pp. 64-74, 2011.

[45] J. Fontanesi, "Youtube.com," Smartscanorange, 13 September 2010. [Online]. Available: http://www.youtube.com/watch?feature=player_embedded&v=K0BdM98LBnc. [Accessed 23 April 2013].

[46] F. E. Boas, "CTmetal artifact artifactreduction reduction and other image post-processing applications," 03 April 2012. [Online]. Available: http://www.stanford.edu/~boas/science/CT/stanford_grand_rounds_talk.pdf. [Accessed 20 04 2013].

[47] B. Menga, J. Wang and L. Xing, "Sinogram preprocessing and binary reconstruction for determination of the shape and location of metal objects in computed tomography (CT)," *American Association of Physicists in Medicine,* vol. 37, no. 11, pp. 5867-5875, 2010.

[48] O. Watzke, “imp.uni-erlangen.de,” Institute of Medical Physics, Erlangen, Germany, 2013.

[49] L. Gallo, M. Brasi, B. Ernst and S. Palla, “Relevance of mandibular helical axis analysis in functional and dysfunctional TMJs,” *Journal of Biomechanics,* vol. 39, pp. 1716-1725, 2005.

[50] E. Lemley, “Engineering Fundamentals, Linear Interpolation in Engineering,” evan.lemley.org, Oklahoma, 2009.

[51] M. Lin, “Academic Life in Emergency Medicine,” noaesthetic.com, 31 July 2012. [Online]. Available: http://academiclifeinem.blogspot.fi/2012_07_01_archive.html. [Accessed 04 May 2013].

[52] R. Gonzalez and R. Woods, Digital Image Processing, Jersey: Prentice-Hall Inc., 2002.

[53] Z. Wang, A. C. Bovik, H. R. Sheikh and E. P. Simoncelli, “Image Quality Assessment: From Error Visibility to Structural Similarity,” *IEEE Transactions on Image Processing,* vol. 13, no. 4, pp. 1-14, 2004.

[54] Z. Wang, A. C. Bovik, H. R. Sheikh and E. P. Simoncelli, “ The SSIM Index for Image Quality Assessment,” Electrical and Electronics Engineering Department, University of Waterloo, 20 January 2012. [Online]. Available: https://ece.uwaterloo.ca/~z70wang/research/ssim/. [Accessed 20 04 2013].

[55] W. v. Aarle, K. J. Batenburg and J. Sijbers, “Optimal threshold selection for segmentation of dense homogeneous objects in tomographic reconstructions,” *Transactions on Medical Imaging,* pp. 1-10, 2011.

[56] N. Otsu, “A threshold selection method from gray level histograms,” *IEEE Transactions on Systems, Man and Cybernetics,* vol. 9, pp. 62-66, 1979.

[57] X. Yu and J. Ylaaski, “A new algorithm for image segmentation based in region growing and edge detection,” *Proc. Int. Symp. Circuits and Systems,* vol. 1, pp. 516-519, 1991.

[58] F. M. S. Beucher, “The morphological approach to segmentation: the watershed transformation,” *Mathematical Morphology in Image Processing.,* 1993 1993.

[59] M. Meilinger, “Metal Artifact Reduction and Image Processing of Cone-Beam Computed Tomography Data for Mobile C-Arm CT Devices,” Universität Regensburg, Regensburg, 2010.

[60] B. S. Morse, “University of Edinburgh School of Informatics,” 12 January 2000. [Online]. Available:

http://homepages.inf.ed.ac.uk/rbf/CVonline/LOCAL_COPIES/MORSE/threshold.pdf. [Accessed 19 March 2013].

[61] S. Tohnak, A. Mehnert, M. Mahoney and S. Crozier, "Dental CT metal artefact reduction based on sequential substitution," Dentomaxillofacial Radiology, 2011.

[62] M. Bertalmio, G. Sapiro, V. Caselles and C. Ballester, "Image Inpainting," in *Proceedings of the 27th annual conference on computer graphics and interactive techniques*, New York, 2000.

[63] Y. Kim, S. Yoon and J. Yi, "Effective Sinoogram Inpinting for Metal Artifact Reduction," in *IEEE 17th International Conference on Image Processing*, 2010.

[64] U. Tuna, S. Peltonen and U. Ruotsalainen, "Gap Filling for the High Resolution PET Sinograms With Dedicated DCT Domain Filter," *IEEE Transactions on Medical Imaging,* vol. 29, no. 3, pp. 830-839, 2010.

[65] U. Tuna and U. Ruotsalainen, "Metal Artifact Reduction With DCT-Domain Gap-Filling Method," in *IEEE Nuclear Science Symposium and Medical Imaging Conference*, California, 2012.

[66] S. Singh, M. K. Kalra, J. Hsieh and P. E. Licato, "Abdominal CT: Comparison of Adaptive Statistical Iterative and Filtered Back ProjectionReconstruction Techniques," *Radiology*, vol. 257, no. 2, pp. 373-383, 2010.

[67] U. Tuna, D. Us and U. Ruotsalainen, "Metal Artifact Reduction Based on Multi-Level Sinogram Segmentation and Sequentially Applied MAP-EM Reconstruction Method," in *2013 IEEE Nuclear Science Symposium and Medical Imaging Conference*, Saeul, 2013. Submitted on May 2013.

APPENDIX 1: Current CBCT equipment

Current commercially available CBCT equipment [28]

Unit	Model(s)	Manufacturer/Distributor
Accuitomo	3D Accuitomo—XYZ Slice View Tomograph/Veraviewpacs 3D	J. Morita Mfg. Corp., Kyoto, Japan
Asahi Roentgen	PSR 9000N (Alphard 3030)	Asahi Roentgen, Kyoto, Japan/Distributed by Belmont, Somerset, NJ, USA
Galileos	Galileos	Sirona Dental Systems, Charlotte, NC, USA
GENDEX	CB 500	Imaging Sciences International, Hatfield, PA, USA/Distributed by Gendex, Chicago, IL, USA
Hitachi	CB MercuRay/CB Throne	Hitachi Medical Corp., Chiba-ken, Japan
iCAT	Classic/Next Generation	Imaging Sciences International, Hatfield, PA, USA
ILUMA	Ultra Cone Beam CT Scanner	IMTEC Imaging Ardmore, OK, USA/Distributed by GE Healthcare, Piscataway, NJ, USA
KaVo	3D eXam	Imaging Sciences International, Hatfield, PA, USA/Distributed by KaVo Dental Corp., Biberach, Germany
KODAK	9000 3D/9500 3D	KODAK Dental Systems, Carestream Health Rochester NY, USA/Distributed exclusively in the USA by PracticeWorks, Atlanta, GA, USA
Newtom	3G/NewTom VG	QR, Inc. Verona, Italy/Dent-X Visionary Imaging, Elmsford, NY, USA
ORION	RCB-888	Ritter Imaging GmbH, Ulm, Germany
Picasso Series	Trio/Pro/Master	E-Woo Technology Co., Ltd/Vatech, Giheung-gu, Korea
PreXion	3D	PreXion, Inc. San Mateo, CA, USA
Promax	3D	Planmeca OY, Helsinki, FInland
Ritter	Orion RCB-888	Ritter Imaging GmbH, Ulm, Germany
Scanora	Scanora 3D CBCT	SOREDEX, Tuusula, Finland
SkyView	3D Panoramic imager	My-Ray Dental Imaging, Cefla Dental Group, Imola, Italy
Suni	3D	Suni Corp., CA, USA
TeraRecon	Fine Cube	Yoshida Dental Mfg. Co. Ltd., Tokyo, Japan/Distributed by TeraRecon, Inc., San Mateo, CA, USA

APPENDIX 2: Segmentation Steps

Segmentation steps for Otsu's Thresholding

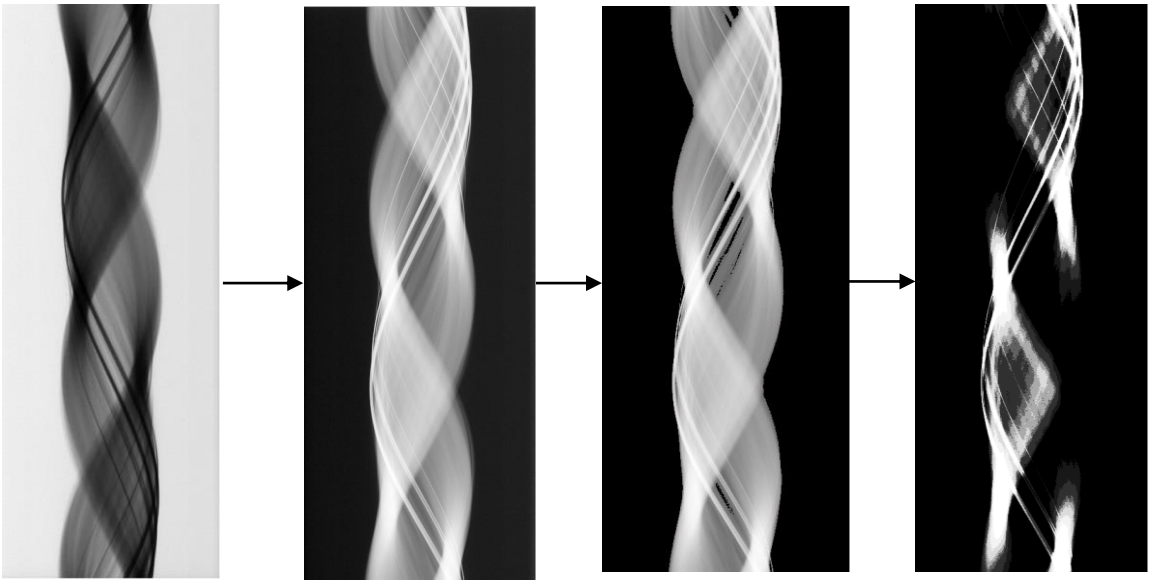

Original sinogram (S_o)

Reversed and normalized sinogram (S_1)

Sinogram after Otsu's thresholding

Averaged sinogram (S_2)

Initial backprojeted image (I_1)

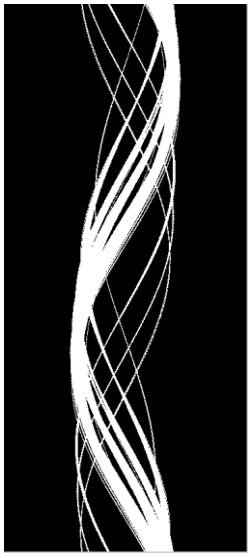

Sinogram mask (S_{mask})

Segmentation steps for Logarithmic Enhancement

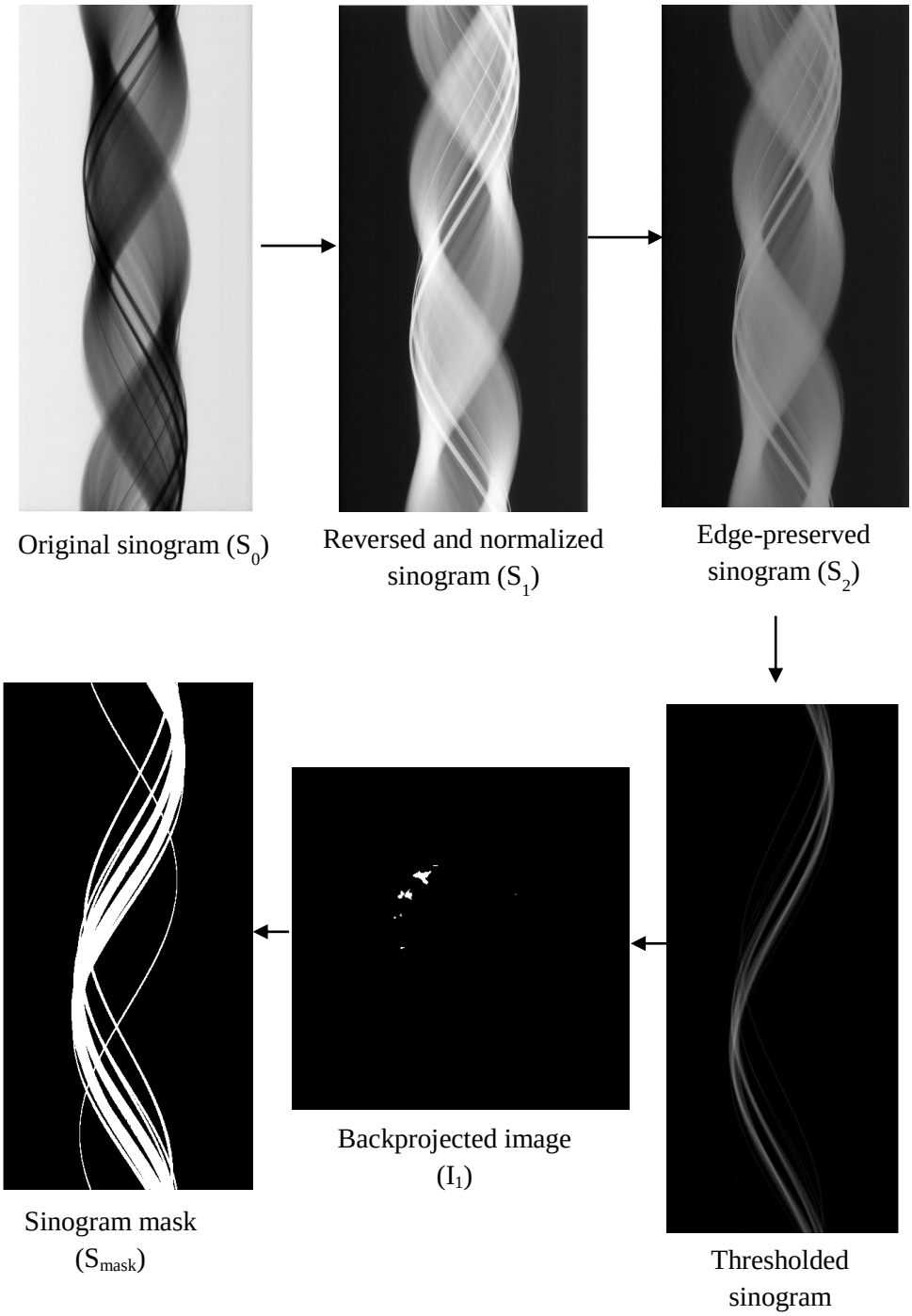

Segmentation steps for K-means Clustering

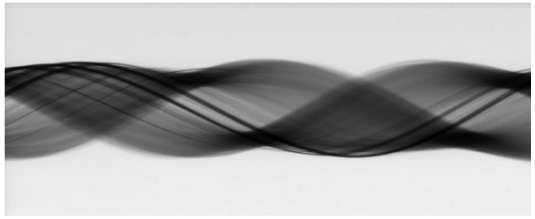

Original sinogram (S_0)

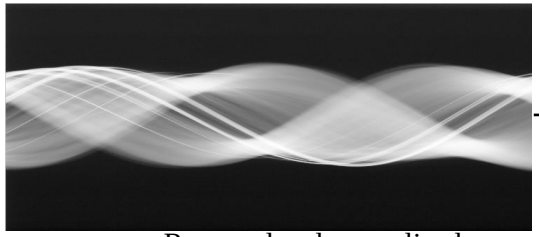

Reversed and normalized sinogram (S_1)

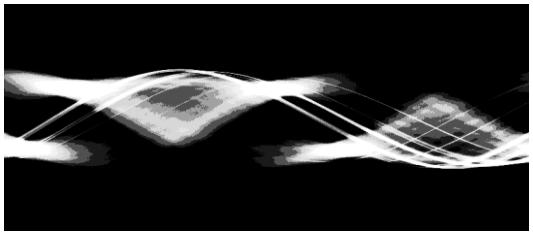

Weighted sinogram (S_2)

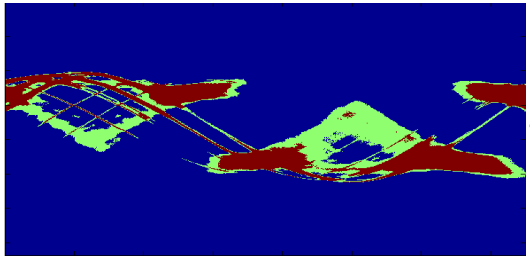

Clustered sinogram (S_3)

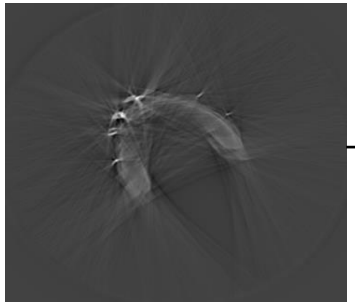

Backprojected image (I_1)

Thresholded I_1 (I_2)

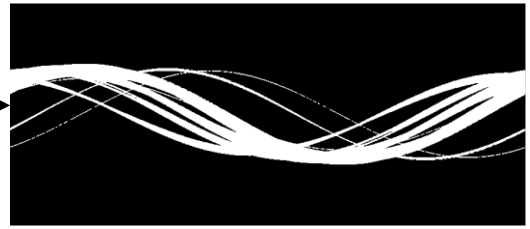

Initial sinogram mask (S_{1mask})

Dilated sinogram mask (S_{mask})